A NURBS-based inverse analysis of thermal expansion induced morphing of thin shells

N. Vu-Bac[c], T.X. Duong[d], T. Lahmer[c], P. Areias[e], R.A. Sauer[d], H.S. Park[f], T. Rabczuk[a,b,*]

[a] *Division of Computational Mechanics, Ton Duc Thang University, Ho Chi Minh City, Viet Nam*
[b] *Faculty of Civil Engineering, Ton Duc Thang University, Ho Chi Minh City, Viet Nam*
[c] *Institute of Structural Mechanics, Bauhaus-Universität Weimar, Marienstr. 15, D-99423 Weimar, Germany*
[d] *Aachen Institute for Advanced Study in Computational Engineering Science (AICES), RWTH Aachen University, Templergraben 55, 52056 Aachen, Germany*
[e] *Department of Physics, Colégio Luís António Verney, University of Évora, Rua Romão Ramalho, 59, 7002-554 Évora, Portugal*
[f] *Department of Mechanical Engineering, Boston University, Boston, MA 02215, USA*
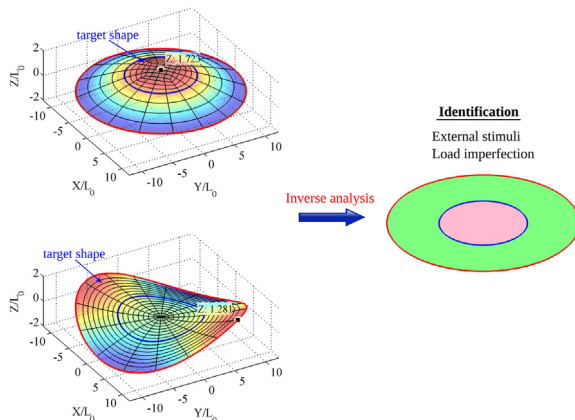
Highlights

- An inverse analysis is used to reconstruct deformations of geometric composites.
- A multiplicative decomposition of the surface deformation is formulated.
- Thermal expansion induced shape changes involving elastic softening are considered.

Graphical Abstract

Abstract

Soft, active materials have been widely studied due to their ability to undergo large, complex shape changes in response to both mechanical and non-mechanical external stimuli. However, the vast majority of such studies has focused on investigating

---

* Corresponding author.
  E-mail address: timon.rabczuk@tdtu.edu.vn (T. Rabczuk).

the forward problem, i.e. determining the shape changes that result from the applied stimuli. In contrast, very little work has been done to solve the inverse problem, i.e. that of identifying the external loads and stimuli that are needed to generate desired shapes and morphological changes. In this work, we present a new inverse methodology to study residual thermal expansion induced morphological changes in geometric composites made of soft, thin shells. In particular, the method presented in this work aims to determine the prescribed external stimuli needed to reconstruct a specific target shape, with a specific focus and interest in morphological changes from two-dimensional (2D) to three-dimensional (3D) shapes by considering the external stimuli within a thermohyperelastic framework. To do so, we utilize a geometrically exact, rotation-free Kirchhoff–Love shell formulation discretized by NURBS-based shape functions. We show that the proposed method is capable of identifying the stimuli, including cases where thermal expansion induced shape changes involving elastic softening occur in morphing from the initially flat 2D to non-planar 3D shapes. Validation indicates that the reconstructed shapes are in good agreement with the target shape.

1. Introduction

Non-mechanical stimuli such as heating, swelling or differential growth have noticeable effects on the morphology of slender structures. Especially, soft materials in the form of membranes [1,2] can be mechanically deformed in response to these stimuli. As the membranes are thin, even small volume changes can cause a drastic shape change, i.e. the fast closure mechanism of the Venus flytrap's leaves after osmotic swelling [3] or the ventral furrow formation in Drosophila [4]. Furthermore, mechanical instabilities can be induced by these stimuli that lead to structural failure [5]. Since mechanical instabilities and shape changes are crucial during the morphogenesis of biological structures [6,7], it is critical to understand how these stimuli lead to specific shape changes.

It was realized by Pezzulla et al. [8] that residual swelling-induced large deformation in a thin structure has significant potential as a technique for shape-morphing design. In this technique, if specific areas within a thin membrane are subject to local swelling, the membrane can morph into a new shape. By suitably preparing geometric composite membranes and locally adjusting their intrinsic geometry, growth-like morphing of 2D membranes to nontrivial 3D shapes under residual swelling can be controlled. Geometric composites refer to combinations of different intrinsic geometries, like an annulus or circular disk, that are different from individual components [9]. They describe the swelling dynamics as a diffusive processes with a Fourier-like differential equation (e.g. Fick's law), and thus the morphing of geometric composites is governed by both swelling and geometry. While the former is induced and controlled by diffusion, the latter dictates deformation of the body (membrane). As reported in [10], flat membranes can be deformed to adopt dome-like [11] or saddle-like shapes [8] when swelling develops within the mid-surface of the membranes. Alternatively, when swelling acts through the thickness, the membranes can bend into cylindrical shapes [12].

Various theories have been developed to study the morphing of thin, soft structures such as buckling of swelling gels [13] and sheets [14,15]. Non-Euclidean shell theory has been extended recently to describe the deformation mechanism of thin, soft objects subjected to external stimuli [16]. Kirchhoff–Love shell theory is ideal for modeling thin shell structures. However, since Kirchhoff–Love shell formulations cannot be solved with standard finite elements that are only C^0-continuous, NURBS-based finite element discretizations are employed [17,18]. Furthermore, because of their ability to model complex geometries and to avoid rotational degrees of freedom, NURBS-based discretizations have recently been used in shape and topology optimizations [19–22].

A well known problem in computational shell formulations is locking. According to Bischoff et al. [23], locking occurs when a finite element formulation is unable to represent certain deformation modes without undesirable parasitic strains or stresses. Several types of locking exist: (1) Poisson thickness locking, (2) membrane locking, (3) volume locking, (4) curvature thickness locking, (5) shear locking as reported in [24]. Due to a negligible effect of the related mechanical phenomena, specific plate or shell models may be unaffected by locking. For example, Kirchhoff–Love shells do not experience transverse shear-locking occurring in solids and shear-deformable shells in the limit of vanishing thickness, see [25]. Echter et al. [26] developed a new class of NURBS-based shell and solid finite elements. Their formulation is based on the discrete shear gap (DSG) method. Examples of locking problems are examined and it is shown that the resulting NURBS DSG elements are completely locking-free. Then,

a hierarchic family of NURBS-based shell finite elements was proposed where the curvature thickness locking is removed. By applying two sequential approaches, DSG and hybrid-mixed method derived from the Hellinger–Reissner variational principle to prevent parasitic membrane strains, membrane locking and in-plane shear locking are eliminated in [27]. Leonetti et al. [28] proposed a method where the Green–Lagrange strains are linearized through the thickness so that a modified generalized constitutive matrix can be adopted. Consequently, thickness locking is prevented and accurate results are obtained without introducing additional degrees of freedom.

Along with the challenges in modeling the deformation of thin structures, there are additional complexities involved in modeling soft materials, as shape changes of soft structures can be induced by swelling, drying, squeezing and permeation [29]. Therefore, a fully coupled deformation-diffusion theory is required to account for the response of the soft materials more accurately [30]. Early studies of swelling of soft matter were carried out by Tanaka et al. [31]. Following this, several studies of swelling-induced deformations in responsive material have been developed [30,32,33] for understanding the physical mechanisms governing shape-morphing.

However, most studies on soft active materials have focused on the forward problem, i.e. determining the shape changes in response to different applied stimuli [5,8,12,16,34]. In contrast, there has been little work done to solve the inverse problem, i.e. determining the external loads and stimuli that are necessary to generate desired shape and morphological changes. Therefore, we propose in this work an inverse methodology to determine the non-mechanical loads and stimuli that are needed to generate a specific 3D shape from an initially flat 2D thin sheet. The approach combines NURBS-based FE discretizations to capture the higher order surface continuity requirements for Kirchhoff–Love shells with a thermohyperelastic framework accounting for non-mechanical stimuli. Our formulation is the first thermomechanical FE formulation for shells based on a multiplicative decomposition of the surface deformation. We demonstrate the ability to reconstruct the target shapes of geometric composite shells where the shape changes occur via swelling (or thermal expansion) induced softening.

The article is organized as follows. In Section 2 the kinematics and the thermomechanical multiplicative decomposition of the deformation gradient are briefly summarized. In the next section, the governing partial differential equations, constitutive equations, weak form and linearizations for the thermomechanical coupled model are presented. The FE formulation follows in Section 4. Rotational constraints are described in Section 4.3. Section 5 describes the inverse analysis using gradient-based methods with analytical sensitivities. The proposed formulation is verified and illustrated through numerical examples in Section 6. In particular, swelling (or thermal expansion) induced softening like buckling is taken into consideration. Finally, the article closes with concluding remarks.

2. A brief description of thin shell theory

2.1. Thin shell kinematics and deformation

A general surface $\mathcal{S}$, shown in Fig. 1, is described by the parametric mapping of the 2D coordinates (ξ^1, ξ^2) to point $\boldsymbol{x}$ in the spatial domain as follows

$$\boldsymbol{x} = \boldsymbol{x}(\xi^\alpha), \quad \alpha = 1, 2, \tag{1}$$

where ξ^α with $\alpha = 1, 2$ denotes the coordinates in the parameter domain $\mathcal{P}$. Lower case symbols are used to denote kinematical quantities, like $\boldsymbol{x}$, in the current configuration $\mathcal{S}$, while upper case symbols are used for the reference configuration $\mathcal{S}_0$. The respective covariant base vectors are then defined by differentiation of $\boldsymbol{x}$ and $\boldsymbol{X}$ with respect to ξ^α as

$$\boldsymbol{a}_\alpha = \frac{\partial \boldsymbol{x}}{\partial \xi^\alpha} \quad \text{and} \quad \boldsymbol{A}_\alpha = \frac{\partial \boldsymbol{X}}{\partial \xi^\alpha}. \tag{2}$$

The corresponding unit normal vectors are determined by $\boldsymbol{n} = (\boldsymbol{a}_1 \times \boldsymbol{a}_2)/\|\boldsymbol{a}_1 \times \boldsymbol{a}_2\|$ for $\mathcal{S}$ and $\boldsymbol{N} = (\boldsymbol{A}_1 \times \boldsymbol{A}_2)/\|\boldsymbol{A}_1 \times \boldsymbol{A}_2\|$ for $\mathcal{S}_0$. From the covariant base vectors, the covariant metric of the midsurface

$$\begin{aligned} A_{\alpha\beta} &= \boldsymbol{A}_\alpha \cdot \boldsymbol{A}_\beta, \\ a_{\alpha\beta} &= \boldsymbol{a}_\alpha \cdot \boldsymbol{a}_\beta, \end{aligned} \tag{3}$$

and the contravariant metric $[A^{\alpha\beta}] = [A_{\alpha\beta}]^{-1}$ and $[a^{\alpha\beta}] = [a_{\alpha\beta}]^{-1}$ can be evaluated. Then, the contravariant base vectors are determined by $\boldsymbol{A}^\alpha = A^{\alpha\beta} \boldsymbol{A}_\beta$ and $\boldsymbol{a}^\alpha = a^{\alpha\beta} \boldsymbol{a}_\beta$. The covariant components of the curvature tensor are
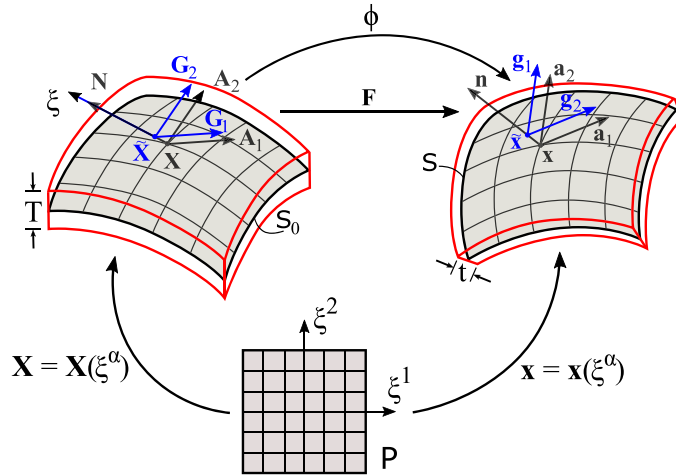
Fig. 1. The definition of reference ($\mathcal{S}_0$) and deformed ($\mathcal{S}$) surfaces. Mapping of the surface parameters (ξ^1, ξ^2) to material points X and spatial points x. The covariant base and the unit normal vectors at $\tilde{X}$ and $\tilde{x}$ in the shell continuum are denoted by $\mathbf{G}_\alpha$, $\mathbf{G}_3$ and $\mathbf{g}_\alpha$, $\mathbf{g}_3$, respectively.
Source: The figure is adopted from [37].

given by

$$B_{\alpha\beta} = N \cdot A_{\alpha,\beta},$$
$$b_{\alpha\beta} = n \cdot a_{\alpha,\beta}. \tag{4}$$

With this, the respective mean, Gaussian and principal curvatures of surface $\mathcal{S}$ are provided by

$$H = \frac{1}{2} a^{\alpha\beta} b_{\alpha\beta}, \quad \kappa = \frac{\det[b_{\alpha\beta}]}{\det[a_{\alpha\beta}]}, \quad \kappa_{1/2} = H \pm \sqrt{H^2 - \kappa}. \tag{5}$$

The mapping $X \to x$, denoted $x = \phi(X)$, is characterized by the surface deformation gradient

$$F := a_\alpha \otimes A^\alpha, \tag{6}$$

The Green–Lagrange strain and the curvature tensors of the mid-surface are provided in [35,36] as follows

$$E = E_{\alpha\beta} A^\alpha \otimes A^\beta = \frac{1}{2} \left(a_{\alpha\beta} - A_{\alpha\beta} \right) A^\alpha \otimes A^\beta,$$
$$K = K_{\alpha\beta} A^\alpha \otimes A^\beta = \left(b_{\alpha\beta} - B_{\alpha\beta} \right) A^\alpha \otimes A^\beta. \tag{7}$$

2.2. Multiplicative decomposition $F = F_M F_\theta$

The Kirchhoff–Love shell shown in Fig. 1 is subjected to mechanical loads and temperature variation. The steady-state thermohyperelastic response is described by the full coupling of the nonlinear mechanical equilibrium equation with the heat transfer equation. The coupling is also manifested in the total surface deformation gradient F consisting of mechanical and thermal terms. Furthermore, the heat transfer equation is solved on the current configuration that also contributes to the coupling. The total surface deformation gradient F of Eq. (6) can be multiplicatively decomposed into a purely mechanical F_M and a purely thermal F_θ portion [38] as

$$F = F_M F_\theta. \tag{8}$$

Here, the thermal part is assumed to be isotropic so that the thermal deformation gradient F_θ can be described by

$$F_\theta = \varphi I, \tag{9}$$

with $I = A_\alpha \otimes A^\alpha$ being the surface identity tensor on $\mathcal{S}_0$ and
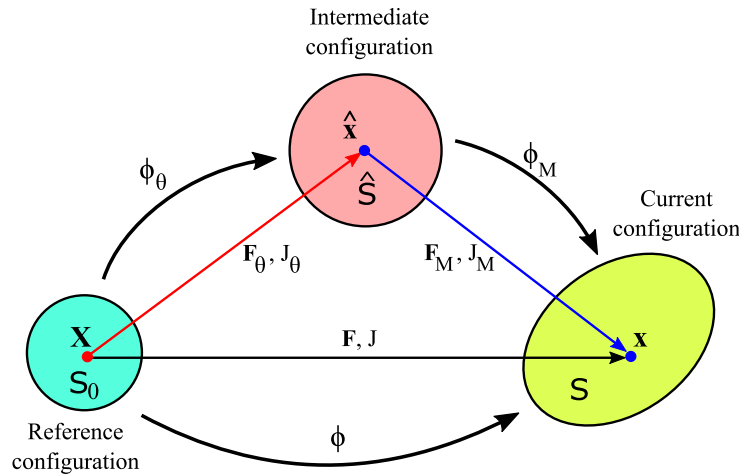
$$\varphi := 1 + \alpha_\theta \left(\theta - \theta_0 \right), \tag{10}$$

Fig. 2. Sketch of multiplicative decomposition $\boldsymbol{F} = \boldsymbol{F}_M \boldsymbol{F}_\theta$.
Source: This figure is adopted from [39].

where α_θ is the *thermal expansion coefficient*, θ_0 is a reference temperature and θ is the temperature in the current configuration. The area change associated with free thermal expansion is characterized by

$$J_\theta = \det{}_s(\boldsymbol{F}_\theta) = \varphi^2 = (1 + \alpha_\theta(\theta - \theta_0))^2. \tag{11}$$

Here, $\det_s$ denotes the surface determinant. The total deformation gradient can be expressed as

$$J = \frac{J_a}{J_A} = \frac{\sqrt{\det[a_{\alpha\beta}]}}{\sqrt{\det[A_{\alpha\beta}]}} = J_M J_\theta. \tag{12}$$

The mechanical surface deformation gradient $\boldsymbol{F}_M$ and the mechanical area change J_M can then be computed from the total surface deformation gradient and the temperature as

$$\boldsymbol{F}_M = \boldsymbol{F}\boldsymbol{F}_\theta^{-1} = \boldsymbol{a}_\alpha \otimes \hat{\boldsymbol{a}}^\alpha \quad \text{and} \quad J_M = \frac{J}{J_\theta} = \frac{J}{[1 + \alpha_\theta(\theta - \theta_0)]^2}, \tag{13}$$

which will be adopted in the definition of the mechanical free-energy. Here we have introduced base vectors $\hat{\boldsymbol{a}}_\alpha = \varphi \boldsymbol{A}_\alpha$, $\hat{\boldsymbol{a}}^\alpha = (1/\varphi)\boldsymbol{A}^\alpha$ associated with the intermediate configuration $\hat{\mathcal{S}}$, see Fig. 2. Other quantities such as the metric tensors $\hat{a}_{\alpha\beta}$, $\hat{a}^{\alpha\beta}$, $\hat{b}_{\alpha\beta}$ and $\hat{b}^{\alpha\beta}$ are computed in the same manner as their counterparts presented in Section 2.1. The right surface Cauchy–Green tensors are determined as

$$\boldsymbol{C} = \boldsymbol{F}^T \boldsymbol{F} = a_{\alpha\beta} \, \boldsymbol{A}^\alpha \otimes \boldsymbol{A}^\beta, \quad \boldsymbol{C}_M = \boldsymbol{F}_M^T \boldsymbol{F}_M = a_{\alpha\beta} \, \hat{\boldsymbol{a}}^\alpha \otimes \hat{\boldsymbol{a}}^\beta. \tag{14}$$

Furthermore, the mechanical surface Green–Lagrange strain and the mechanical relative curvature tensors can be defined by

$$\begin{aligned}
\boldsymbol{E}_M &= \frac{1}{2}(\boldsymbol{C}_M - \boldsymbol{I}) = \varepsilon_{\alpha\beta}^M \, \hat{\boldsymbol{a}}_\alpha \otimes \hat{\boldsymbol{a}}_\beta = \frac{1}{2}\left(a_{\alpha\beta} - \hat{a}_{\alpha\beta}\right)\hat{\boldsymbol{a}}^\alpha \otimes \hat{\boldsymbol{a}}^\beta, \\
\boldsymbol{K}_M &= \kappa_{\alpha\beta}^M \, \hat{\boldsymbol{a}}_\alpha \otimes \hat{\boldsymbol{a}}_\beta = \left(b_{\alpha\beta} - \hat{b}_{\alpha\beta}\right)\hat{\boldsymbol{a}}^\alpha \otimes \hat{\boldsymbol{a}}^\beta,
\end{aligned} \tag{15}$$

in which we have defined

$$\begin{aligned}
\varepsilon_{\alpha\beta}^M &:= \frac{1}{2}\left(a_{\alpha\beta} - \hat{a}_{\alpha\beta}\right), \\
\kappa_{\alpha\beta}^M &:= b_{\alpha\beta} - \hat{b}_{\alpha\beta}.
\end{aligned} \tag{16}$$

3. A thermomechanical coupled theory

3.1. Governing partial differential equations

In this section, the coupled governing partial differential equations consisting of the balance of forces and the balance of thermal energy are briefly recalled.

3.1.1. Balance of forces

Considering the prescribed body force $\boldsymbol{f}$, the strong form equilibrium equation of the thin shell at $\boldsymbol{x} \in \mathcal{S}$, see [36], is given by

$$\boldsymbol{T}^\alpha_{;\alpha} + \boldsymbol{f} = \boldsymbol{0}, \tag{17}$$

where $\boldsymbol{T}^\alpha_{;\alpha}$ denotes the covariant derivative of $\boldsymbol{T}^\alpha$ with $\boldsymbol{T}^\alpha$ being the internal traction acting on the cross section normal to $\boldsymbol{a}^\alpha$, defined by

$$\boldsymbol{T}^\alpha = \boldsymbol{\sigma}^T \boldsymbol{a}^\alpha = N^{\alpha\beta} \boldsymbol{a}_\beta + S^\alpha \boldsymbol{n}, \tag{18}$$

with $\boldsymbol{\sigma}$ being the Cauchy stress tensor. The in-plane and shear stress components on the cross section can be expressed as

$$\begin{aligned}
N^{\alpha\beta} &= \sigma^{\alpha\beta} + b^\alpha_\gamma M^{\gamma\beta}, \\
S^\alpha &= -M^{\beta\alpha}_{;\beta},
\end{aligned} \tag{19}$$

in which membrane stress and moment components $\sigma^{\alpha\beta}$ and $M^{\alpha\beta}$ are given in Section 3.2. On the boundary $\partial\mathcal{S} = \partial_x\mathcal{S} \cup \partial_t\mathcal{S} \cup \partial_m\mathcal{S}$, the Dirichlet and Neumann boundary conditions are

$$\begin{aligned}
\boldsymbol{x} &= \bar{\boldsymbol{\phi}}, & &on \ \partial_x\mathcal{S}, \\
\boldsymbol{t} &= \bar{\boldsymbol{t}}, & &on \ \partial_t\mathcal{S}, \\
m_\tau &= \bar{m}_\tau, & &on \ \partial_m\mathcal{S},
\end{aligned} \tag{20}$$

where $\bar{\boldsymbol{\phi}}$, $\bar{\boldsymbol{t}} = \bar{t}^\alpha \boldsymbol{a}_\alpha$, and $\bar{m}_\tau$ are prescribed boundary deformations, tractions and bending moments parallel to boundary $\partial\mathcal{S}$, respectively.

3.1.2. Balance of energy

According to Sahu et al. [40], the local form of the internal surface energy balance is generally described by

$$\dot{\varXi} = -q^\alpha_{;\alpha} + Q + \frac{1}{2}\sigma^{\alpha\beta}\dot{a}_{\alpha\beta} + \frac{1}{2}M^{\alpha\beta}\dot{b}_{\alpha\beta}, \tag{21}$$

where $\varXi$ is the stored energy, $q^\alpha_{;\alpha}$ is the covariant derivative of q^α, which is the contravariant component of the heat flux $\boldsymbol{q}$ on $\mathcal{S}$ and Q denotes the heat source per unit time. The last two terms on the right hand side denote the internal stress power. Since this study is interested in steady-state solutions, the governing equation for heat conduction on surface can be rewritten as:

$$q^\alpha_{;\alpha} = Q \tag{22}$$

The boundary conditions consist of the prescribed temperature $\bar{\theta}$ on $\partial_\theta\mathcal{S}$ and the prescribed heat flux $\bar{q}$ on $\partial_q\mathcal{S}$ as

$$\theta = \bar{\theta} \quad on \quad \partial_\theta\mathcal{S}, \tag{23}$$

$$q_\nu = -q^\alpha \nu_\alpha = \bar{q} \quad on \quad \partial_q\mathcal{S} \tag{24}$$

where $\nu_\alpha = \boldsymbol{\nu} \cdot \boldsymbol{a}_\alpha$ denotes the covariant component of the boundary normal $\boldsymbol{\nu}$.

Remark. The transport equation for the concentration is given by

$$\frac{\partial c}{\partial t} + j^\alpha_{;\alpha} = S \tag{25}$$

where $j^\alpha_{;\alpha}$ is the covariant derivative of j^α, which is the contravariant component of the molar flux $\boldsymbol{j}$, t denotes time and S is the surface source term. The transport equation is independent of the stress power. The molar flux due to diffusion can be described by Fick's law as follows

$$j^\alpha = -D \, a^{\alpha\beta} \, c_{;\beta} \tag{26}$$

with c being the concentration and D being the diffusion coefficient. The hygroscopic swelling stretch is given by

$$\varphi_c = 1 + \alpha_c(c - c_0), \tag{27}$$

where α_c is coefficient of hygroscopic swelling and c_0 is the initial concentration in the system. The transport equation governing concentration gradients, Eq. (25), is then solved for the concentration in the system (like the geometric composite disk of Section 6) and then the concentration gradient provides a thermal-like strain. Note that the strain rate does not affect the transport equation.

Due to the similarity between the heat conduction, Eq. (21), and diffusion, Eq. (25), swelling is analogous to a thermal strain, but driven by a concentration gradient instead of a temperature gradient.

3.2. Constitutive equations

This study focuses on the quasi-static behavior of soft materials that can be described by a thermohyperelastic model. We assume there exists a corresponding Helmholtz free energy of the form $W = W(\boldsymbol{E}_M, \boldsymbol{K}_M, \theta)$ defined per unit intermediate area. The constitutive equations for the Kirchhoff stress and the bending moment associated with the intermediate configuration $\hat{\mathcal{S}}$ are then defined by [38]

$$\tau^{\alpha\beta}_M := \frac{\partial W}{\partial \varepsilon^M_{\alpha\beta}} = 2\frac{\partial W}{\partial a_{\alpha\beta}},$$
$$M^{\alpha\beta}_M := \frac{\partial W}{\partial \kappa^M_{\alpha\beta}} = \frac{\partial W}{\partial b_{\alpha\beta}}. \tag{28}$$

Pushing forward $\tau^{\alpha\beta}_M$ and $M^{\alpha\beta}_M$ from $\hat{\mathcal{S}}$ to $\mathcal{S}$, leads to the Cauchy stress $\sigma^{\alpha\beta}$ and moment $M^{\alpha\beta}$ given by

$$\sigma^{\alpha\beta} = \frac{1}{J_M}\tau^{\alpha\beta}_M$$
$$M^{\alpha\beta} = \frac{1}{J_M}M^{\alpha\beta}_M. \tag{29}$$

In the following, the Koiter material model and an incompressible Neo-Hookean model are used to account for the mechanical energy and the Fourier law is used within the heat equation. It should be noted that the material properties are taken as independent of the temperature in this study.

3.2.1. Koiter material model

The Koiter material model [41] describes the surface strain energy, corresponding to $\boldsymbol{F}_M$, as follows

$$W = \frac{1}{8} \left(a_{\alpha\beta} - \hat{a}_{\alpha\beta}\right) \hat{c}^{\alpha\beta\gamma\delta} \left(a_{\gamma\delta} - \hat{a}_{\gamma\delta}\right) + \frac{1}{2} \left(b_{\alpha\beta} - \hat{b}_{\alpha\beta}\right) \hat{f}^{\alpha\beta\gamma\delta} \left(b_{\gamma\delta} - \hat{b}_{\gamma\delta}\right), \tag{30}$$

with the material tangents

$$\hat{c}^{\alpha\beta\gamma\delta} = \Lambda\hat{a}^{\alpha\beta}\hat{a}^{\gamma\delta} + \mu \left(\hat{a}^{\alpha\gamma}\hat{a}^{\beta\delta} + \hat{a}^{\alpha\delta}\hat{a}^{\beta\gamma}\right),$$
$$\hat{f}^{\alpha\beta\gamma\delta} = \frac{T^2}{12}\hat{c}^{\alpha\beta\gamma\delta}, \tag{31}$$

where T denotes the shell thickness at the intermediate configuration $\hat{\mathcal{S}}$; Λ and μ are the Lamé constants. The Kirchhoff stress and moment follow from Eq. (28) as

$$\tau^{\alpha\beta}_M = \frac{1}{2}\hat{c}^{\alpha\beta\gamma\delta} \left(a_{\gamma\delta} - \hat{a}_{\gamma\delta}\right),$$
$$M^{\alpha\beta}_M = \hat{f}^{\alpha\beta\gamma\delta} \left(b_{\gamma\delta} - \hat{b}_{\gamma\delta}\right). \tag{32}$$

Alternative stress measures $\sigma^{\alpha\beta}$ and $M^{\alpha\beta}$ shown in Eq. (29) can be then obtained.

3.2.2. Shell constitutive model derived from 3D material models

In this section, the formulation of Kirchhoff–Love shell constitution is established by projecting a 3D model onto the surface $\mathcal{S}$ as depicted in Fig. 1. By doing so, an arbitrary point P in 3D continuum can be expressed as

$$
\begin{aligned}
\tilde{X}(\xi^\alpha, \xi) &= x(\xi^\alpha) + \xi N(\xi^\alpha) \\
\tilde{x}(\xi^\alpha, \xi) &= X(\xi^\alpha) + \xi d(\xi^\alpha),
\end{aligned}
\tag{33}
$$

with $\xi \in [-T/2\ \ T/2]$ being the thickness coordinate and T denoting the shell thickness. If we denote λ_3 as the stretch in the normal direction, the director vector can be written as $d := \lambda_3 n$. Hence, the metric tensors at point P now can be written in terms of their counterparts on the mid-surface as follows:

$$
\begin{aligned}
g_{\alpha\beta} &= g_a\, a_{\alpha\beta} + g_b\, b_{\alpha\beta}, \quad \hat{g}_{\alpha\beta} = \hat{g}_a\, \hat{a}_{\alpha\beta} + \hat{g}_b\, \hat{b}_{\alpha\beta}, \\
g^{\alpha\beta} &= g^a\, a^{\alpha\beta} + g^b\, b^{\alpha\beta}, \quad \hat{g}^{\alpha\beta} = \hat{g}^a\, \hat{a}^{\alpha\beta} + \hat{g}^b\, \hat{b}^{\alpha\beta}.
\end{aligned}
\tag{34}
$$

Here,

$$
\begin{aligned}
g_a &:= 1 - \xi^2 \kappa, \quad g_b := 2\xi + 2H\xi^2, \\
\hat{g}_a &:= 1 - \xi^2 \hat{\kappa}, \quad \hat{g}_b := 2\xi + 2\hat{H}\xi^2, \\
g^a &:= s^{-2}(g_a + 2Hg_b), \quad g^b := -s^{-2}g_b, \\
\hat{g}^a &:= \hat{s}^{-2}(\hat{g}_a + 2\hat{H}\hat{g}_b), \quad \hat{g}^b := -\hat{s}^{-2}\hat{g}_b,
\end{aligned}
\tag{35}
$$

in which

$$
s = 1 + 2H\xi + \kappa\xi^2, \quad \hat{s} = 1 + 2\hat{H}\xi + \hat{\kappa}\xi^2.
\tag{36}
$$

The projected Kirchhoff stress and moment now yield

$$
\begin{aligned}
\tau^{\alpha\beta} &= \int_{-\frac{T}{2}}^{\frac{T}{2}} \hat{s}\left(1 - \xi^2\kappa\right)\, \tilde{\tau}^{\alpha\beta}\, d\xi, \\
M_0^{\alpha\beta} &= \int_{-\frac{T}{2}}^{\frac{T}{2}} \left(-\xi + H\xi^2\right)\, \tilde{\tau}^{\alpha\beta}\, d\xi,
\end{aligned}
\tag{37}
$$

where $\tilde{\tau}^{\alpha\beta}$ are the 3D Kirchhoff stress components. More details of the projection technique can be found in [37,42].

3.2.3. Incompressible Neo-Hookean material

Introducing the invariants of the 3D Cauchy–Green tensor $\tilde{C}_M$ such that $\tilde{I}_{M1} := \tilde{C}_M : \mathbf{1}$ and $\tilde{J}_M := \sqrt{\det \tilde{C}_M}$ with $\mathbf{1}$ being the identity tensor in $\mathbb{R}^3$, the continuum free energy function (per intermediate volume) of the incompressible Neo-Hookean model has the following form

$$
\tilde{W}(\tilde{I}_{M1}, \tilde{J}_M, p) = \frac{\tilde{\mu}}{2}\left(\tilde{I}_{M1} - 3\right) + p\left(1 - \tilde{J}_M\right),
\tag{38}
$$

with p being the Lagrange multiplier adopted to enforce the incompressibility constraint

$$
g := 1 - \tilde{J}_M = 0.
\tag{39}
$$

The 3D Kirchhoff stress components associated with $\hat{\mathcal{S}}$ thus become

$$
\tilde{\tau}_M^{\alpha\beta} = \tilde{\mu}\left(\hat{g}^{\alpha\beta} - \frac{1}{J_M^{\star 2}}g^{\alpha\beta}\right).
\tag{40}
$$

which are then inserted into Eq. (37) to obtain the projected Kirchhoff stress $\tau_M^{\alpha\beta}$ and moment $M_M^{\alpha\beta}$ through numerical integration. The Cauchy stress $\sigma^{\alpha\beta}$ and moment $M^{\alpha\beta}$ can be obtained using Eq. (29). Hereafter, we will use *Koiter model* to refer to the Koiter material model and the *incompressible Neo-Hookean model* for the projected incompressible Neo-Hookean model for the sake of simplicity.

3.2.4. Constitutive equation for the heat flux

Assuming Fourier's law, the spatial surface heat flux $\boldsymbol{q}$ is related to the spatial surface gradient of the temperature $\theta_{;\beta}$ by

$$q^\alpha = -k \ a^{\alpha\beta} \ \theta_{;\beta}, \tag{41}$$

where k, the scalar surface thermal conductivity, is taken as constant.

3.3. Weak form

3.3.1. Weak form for the mechanical part

The mechanical weak form for the steady-state shell equation (17) is written as: Find $\boldsymbol{x} \in \mathcal{U}$ such that

$$\delta W_x = \delta W_{\text{int}} - \delta W_{\text{ext}} = 0 \quad \forall \delta \boldsymbol{x} \in \mathcal{U}_0, \tag{42}$$

with

$$
\begin{aligned}
\delta W_{\text{int}} &= \int_{\mathcal{S}} \frac{1}{2} \delta a_{\alpha\beta} \ \sigma^{\alpha\beta} \ \text{da} + \int_{\mathcal{S}} \delta b_{\alpha\beta} \ M^{\alpha\beta} \ \text{da}, \\
\delta W_{\text{ext}} &= \int_{\mathcal{S}} \delta \boldsymbol{x} \cdot \boldsymbol{f} \ \text{da} + \int_{\partial_t \mathcal{S}} \delta \boldsymbol{x} \cdot \boldsymbol{t} \ \text{ds} + \int_{\partial_m \mathcal{S}} \delta \boldsymbol{n} \cdot m_\tau \boldsymbol{v} \ \text{ds}.
\end{aligned}
\tag{43}
$$

Alternatively, using Eq. (29) and noting that $\text{da} = J \ \text{dA}$, we can rewrite the internal virtual work δW_{int} as follows

$$\delta W_{\text{int}} = \int_{\mathcal{S}_0} \frac{1}{2} \ \delta a_{\alpha\beta} \ \tau_M^{\alpha\beta} \ J_\theta \ \text{dA} + \int_{\mathcal{S}_0} \delta b_{\alpha\beta} \ M_M^{\alpha\beta} \ J_\theta \ \text{dA}. \tag{44}$$

3.3.2. Weak form for the heat equation

Assuming the heat transfer is quasi-static as shown in Eq. (22). The weak form for the steady-state solution in the deformed surface $\mathcal{S}$ can be stated as: Find $\theta(\boldsymbol{x}) \in \mathcal{V}$ such that

$$\delta W_\theta = \delta W_{\text{int}\theta} - \delta W_{\text{ext}\theta} = 0, \quad \forall \delta \theta \in \mathcal{V}_0 \tag{45}$$

with

$$
\begin{aligned}
\delta W_{\text{int}\theta} &= \int_{\mathcal{S}} k \ \nabla_{\mathcal{S}} \theta \cdot \nabla_{\mathcal{S}} \delta \theta \ \text{da} \\
\delta W_{\text{ext}\theta} &= - \int_{\partial_q \mathcal{S}} \bar{q} \ \delta \theta \ \text{ds} + \int_{\mathcal{S}} Q \ \delta \theta \ \text{da}.
\end{aligned}
\tag{46}
$$

where $\nabla_{\mathcal{S}} \bullet$ denotes surface gradient of quantity $\bullet$ on $\mathcal{S}$, i.e.

$$
\begin{aligned}
\nabla_{\mathcal{S}} \theta &= \theta_{,\alpha} \boldsymbol{a}^\alpha, \\
\nabla_{\mathcal{S}} \delta \theta &= \delta \theta_{,\alpha} \boldsymbol{a}^\alpha.
\end{aligned}
\tag{47}
$$

3.4. Linearizations

The two weak forms in Eqs. (42) and (45) are solved simultaneously. This results in a coupled system of nonlinear equilibrium equations. To solve these equations, the Newton–Raphson method is employed which requires the linearization of the two equilibrium equations. Linearizing Eq. ((42).1) and Eq. ((45).1) in the direction $\Delta \boldsymbol{x}$ and $\Delta \theta$, we have

$$
\begin{aligned}
\Delta \delta W_{\text{int}} &= \Delta_x \delta W_{\text{int}} + \Delta_\theta \delta W_{\text{int}}, \\
\Delta \delta W_{\text{int}\theta} &= \Delta_x \delta W_{\text{int}\theta} + \Delta_\theta \delta W_{\text{int}\theta},
\end{aligned}
\tag{48}
$$

in which $\Delta_x \bullet$ and $\Delta_\theta \bullet$ denote the linearizations of quantity $\bullet$ with respect to (w.r.t.) x and θ, respectively. The linearization shown by Eq. ((48).1) can be written as

$$
\begin{aligned}
\Delta_x \delta W_{\text{int}} = \int_{\mathcal{S}_0} & \left(\hat{c}^{\alpha\beta\gamma\delta} \, \frac{1}{2} \delta a_{\alpha\beta} \, \frac{1}{2} \Delta_x a_{\gamma\delta} + \hat{d}^{\alpha\beta\gamma\delta} \, \frac{1}{2} \delta a_{\alpha\beta} \, \Delta_x b_{\gamma\delta} + \tau_M^{\alpha\beta} \, \frac{1}{2} \Delta_x \delta a_{\alpha\beta} \right. \\
& \left. + \hat{e}^{\alpha\beta\gamma\delta} \, \frac{1}{2} \delta b_{\alpha\beta} \, \Delta_x a_{\gamma\delta} + \hat{f}^{\alpha\beta\gamma\delta} \, \delta b_{\alpha\beta} \, \Delta_x b_{\gamma\delta} + M_M^{\alpha\beta} \, \Delta_x \delta b_{\alpha\beta} \right) J_\theta \, dA \\
& + \int_{\mathcal{S}_0} \left[\left(\frac{1}{2} \delta a_{\alpha\beta} \, \tau_M^{\alpha\beta} + \delta b_{\alpha\beta} \, M_M^{\alpha\beta} \right) \Delta_\theta J_\theta + \left(\frac{1}{2} \delta a_{\alpha\beta} \, \Delta_\theta \tau_M^{\alpha\beta} + \delta b_{\alpha\beta} \, \Delta_\theta M_M^{\alpha\beta} \right) J_\theta \right] dA,
\end{aligned}
\tag{49}
$$

in which the material tangents are introduced as

$$
\begin{aligned}
\hat{c}^{\alpha\beta\gamma\delta} &:= 2 \frac{\partial \tau_M^{\alpha\beta}}{\partial a_{\gamma\delta}}, \quad \hat{d}^{\alpha\beta\gamma\delta} := \frac{\partial \tau_M^{\alpha\beta}}{\partial b_{\gamma\delta}}, \\
\hat{e}^{\alpha\beta\gamma\delta} &:= 2 \frac{\partial M_M^{\alpha\beta}}{\partial a_{\gamma\delta}}, \quad \hat{f}^{\alpha\beta\gamma\delta} := \frac{\partial M_M^{\alpha\beta}}{\partial b_{\gamma\delta}},
\end{aligned}
\tag{50}
$$

Furthermore, the respective surface gradient of temperature and its variation w.r.t. x and X are related by

$$
\begin{aligned}
\nabla_{\mathcal{S}} \theta &= \boldsymbol{F}^{-T} \, \nabla_{\mathcal{S}_0} \theta \\
\nabla_{\mathcal{S}} \delta\theta &= \boldsymbol{F}^{-T} \, \nabla_{\mathcal{S}_0} \delta\theta.
\end{aligned}
\tag{51}
$$

with $\nabla_{\mathcal{S}_0} \bullet$ being surface gradient of quantity $\bullet$ on $\mathcal{S}_0$. Noticing Eq. (14), the linearization shown by Eq. (48) can be expressed by

$$
\begin{aligned}
\Delta_\theta \delta W_{\text{int}\theta} = \int_{\mathcal{S}_0} & k \, \Delta_x J \, \boldsymbol{C}^{-1} \cdot \nabla_{\mathcal{S}_0} \theta \cdot \nabla_{\mathcal{S}_0} \delta\theta \, dA + \int_{\mathcal{S}_0} k J \, \Delta_x \boldsymbol{C}^{-1} \cdot \nabla_{\mathcal{S}_0} \theta \cdot \nabla_{\mathcal{S}_0} \delta\theta \, dA \\
& + \int_{\mathcal{S}_0} k J \, \boldsymbol{C}^{-1} \cdot \nabla_{\mathcal{S}_0} (\Delta_\theta \theta) \cdot \nabla_{\mathcal{S}_0} \delta\theta \, dA,
\end{aligned}
\tag{52}
$$

The expressions for $\Delta_x \delta a_{\alpha\beta}$ and $\Delta_x \delta b_{\alpha\beta}$ can be found in [41]. Also, the expressions for $\Delta_x J$, $\Delta_x \boldsymbol{C}^{-1}$ are presented in Appendix A and $\Delta_\theta J_\theta$, $\Delta_\theta \tau_M^{\alpha\beta}$, $\Delta_\theta M_M^{\alpha\beta}$ are shown in Appendix B. The linearization of the external virtual works in the equilibrium equation ((43).2) is given by [37,42] as follows

$$
\Delta_x \delta W_{\text{ext}} = \int_{\partial \mathcal{S}} m_\tau \, \delta \boldsymbol{a}_\alpha \cdot \left(\nu^\beta \boldsymbol{n} \otimes \boldsymbol{a}^\alpha + \nu^\alpha \boldsymbol{a}^\beta \otimes \boldsymbol{n} \right) \Delta_x \boldsymbol{a}_\beta \, ds.
\tag{53}
$$

4. Finite element discretization

4.1. FE approximation

The discretization of the surface domain is performed using NURBS-based shape functions, see [43]. The geometry and temperature field within each element domain are approximated using a nodal interpolation as

$$
\boldsymbol{X} \approx \mathbf{N} \, \mathbf{X}_e, \quad \boldsymbol{x} \approx \mathbf{N} \, \mathbf{x}_e,
\tag{54}
$$

in which $\mathbf{N}(\xi^1, \xi^2) := [N_1 \mathbf{1}, \ N_2 \mathbf{1}, \ ..., \ N_{n_e} \mathbf{1}]$ denotes a $(3 \times 3 n_e)$ array shape function, with n_e being the number of nodes, defined on the master element Ω^e in the parametric domain. The covariant tangent vectors of the surfaces are then approximated by

$$
\boldsymbol{A}_\alpha = \frac{\partial \boldsymbol{X}}{\partial \xi^\alpha} \approx \mathbf{N}_{,\alpha} \, \mathbf{X}_e, \quad \boldsymbol{a}_\alpha = \frac{\partial \boldsymbol{x}}{\partial \xi^\alpha} \approx \mathbf{N}_{,\alpha} \, \mathbf{x}_e \quad \text{and} \quad \hat{\boldsymbol{a}}_\alpha = \frac{\partial \hat{\boldsymbol{x}}}{\partial \xi^\alpha} \approx \mathbf{N}_{,\alpha} \, \hat{\mathbf{x}}_e.
\tag{55}
$$

Then, the corresponding unit surface normal vectors can be evaluated. The variation of x and the tangent vector $\boldsymbol{a}_\alpha$ are written as

$$
\delta \boldsymbol{x} \approx \mathbf{N} \, \delta \mathbf{X}_e, \quad \delta \boldsymbol{a}_\alpha \approx \mathbf{N}_{,\alpha} \, \delta \mathbf{x}_e,
\tag{56}
$$

with $\mathbf{N}_{,\alpha}(\xi^1, \xi^2) := [N_{1,\alpha}\mathbf{1}, \ N_{2,\alpha}\mathbf{1}, \ldots, \ N_{n,\alpha}\mathbf{1}]$. Furthermore, the variation of all kinematical quantities shown in Section 2 can be found in [37]. Using the nodal interpolations within element domain Ω^e, the temperature field is approximated by

$$
\begin{aligned}
\theta &\approx \mathbf{N}^\star \ \boldsymbol{\theta}_e, \\
\delta\theta &\approx \mathbf{N}^\star \ \delta\boldsymbol{\theta}_e.
\end{aligned}
\tag{57}
$$

where $\mathbf{N}^\star(\xi^1, \xi^2) := [N_1, \ N_2, \ldots, \ N_n]$ is a $(1 \times n_e)$ array shape function of master element Ω^e; $\boldsymbol{\theta}_e, \delta\boldsymbol{\theta}_e$ are vectors containing the discretized nodal temperature and its variation at element level, respectively. Differentiating Eq. (57) w.r.t. coordinate ξ^α yields the real and virtual temperature gradient interpolation as follows

$$
\begin{aligned}
\theta_{,\alpha} &\approx \mathbf{N}^\star_{,\alpha} \ \boldsymbol{\theta}_e, \\
\delta\theta_{,\alpha} &\approx \mathbf{N}^\star_{,\alpha} \ \delta\boldsymbol{\theta}_e,
\end{aligned}
\tag{58}
$$

Consequently, the surface gradient of the temperature and its variation on $\mathcal{S}$, see [44], are defined by

$$
\begin{aligned}
\nabla_{\mathcal{S}}\theta &= \theta_{,\alpha} \ \boldsymbol{a}^\alpha \approx \boldsymbol{a}^\alpha \ \mathbf{N}^\star_{,\alpha} \ \boldsymbol{\theta}_e, \\
\nabla_{\mathcal{S}}\delta\theta &= \delta\theta_{,\alpha} \ \boldsymbol{a}^\alpha \approx \boldsymbol{a}^\alpha \ \mathbf{N}^\star_{,\alpha} \ \delta\boldsymbol{\theta}_e.
\end{aligned}
\tag{59}
$$

where $\mathbf{N}^\star_{,\alpha}(\xi^1, \xi^2) := [N_{1,\alpha}, \ N_{2,\alpha}, \ldots, \ N_{n_e,\alpha}]$ is an array derivatives of shape function. Likewise, the surface gradient of the temperature and its variation on $\hat{\mathcal{S}}$ and $\mathcal{S}_0$, respectively, can be represented by

$$
\begin{aligned}
\nabla_{\hat{\mathcal{S}}}\theta &= \theta_{,\alpha} \ \hat{\boldsymbol{a}}^\alpha \approx \hat{\boldsymbol{a}}^\alpha \ \mathbf{N}^\star_{,\alpha} \ \boldsymbol{\theta}_e, & \nabla_{\hat{\mathcal{S}}}\delta\theta &= \delta\theta_{,\alpha} \ \hat{\boldsymbol{a}}^\alpha \approx \hat{\boldsymbol{a}}^\alpha \ \mathbf{N}^\star_{,\alpha} \ \delta\boldsymbol{\theta}_e, \\
\nabla_{\mathcal{S}_0}\theta &= \theta_{,\alpha} \ \boldsymbol{A}^\alpha \approx \boldsymbol{A}^\alpha \ \mathbf{N}^\star_{,\alpha} \ \boldsymbol{\theta}_e, & \nabla_{\mathcal{S}_0}\delta\theta &= \delta\theta_{,\alpha} \ \boldsymbol{A}^\alpha \approx \boldsymbol{A}^\alpha \ \mathbf{N}^\star_{,\alpha} \ \delta\boldsymbol{\theta}_e.
\end{aligned}
\tag{60}
$$

where $\nabla_{\hat{\mathcal{S}}}\bullet$ and $\nabla_{\mathcal{S}_0}\bullet$ denote the surface gradient of quantity $\bullet$ on $\hat{\mathcal{S}}$ and $\mathcal{S}_0$, respectively.

4.2. Discretized weak form

Using the above interpolations to discretize the weak form shown by Eq. (43), its approximation reads

$$
\delta W_x \approx \sum_{e=1}^{n_{el}} \delta W_x^e = \sum_{e=1}^{n_{el}} \left(\delta W_{\text{int}}^e - \delta W_{\text{ext}}^e \right),
\tag{61}
$$

where n_{el} is the number of FE elements. The internal and external virtual works associated with the mechanical model per element are approximated by

$$
\begin{aligned}
\delta W_{\text{int}}^e &= \delta\boldsymbol{x}_e^T \left(\mathbf{f}_{\text{int}\tau}^e + \mathbf{f}_{\text{int}M}^e \right), \\
\delta W_{\text{ext}}^e &= \delta\boldsymbol{x}_e^T \left(\mathbf{f}_{\text{ext}0}^e + \mathbf{f}_{\text{ext}p}^e + \mathbf{f}_{\text{ext}t}^e + \mathbf{f}_{\text{ext}m}^e \right).
\end{aligned}
\tag{62}
$$

Here the internal equivalent nodal forces are split into contributions of membrane stress $\tau_M^{\alpha\beta}$ and bending moment $M_M^{\alpha\beta}$ as follows

$$
\begin{aligned}
\mathbf{f}_{\text{int}\tau}^e &:= \int_{\Omega_0^e} \tau_M^{\alpha\beta} \ \mathbf{N}_{,\alpha}^T \boldsymbol{a}_\beta \ J_\theta \ \mathrm{dA}, \\
\mathbf{f}_{\text{int}M}^e &:= \int_{\Omega_0^e} M_M^{\alpha\beta} \left(\mathbf{N}_{,\alpha\beta} - \Gamma_{\alpha\beta}^\gamma \ \mathbf{N}_{,\gamma} \right) \boldsymbol{n} \ J_\theta \ \mathrm{dA},
\end{aligned}
\tag{63}
$$

with $\mathbf{N}_{,\alpha\beta}(\boldsymbol{\xi}) := [N_{1,\alpha\beta}\mathbf{1}, N_{2,\alpha\beta}\mathbf{1}, \ldots, N_{n,\alpha\beta}\mathbf{1}]$ and Christoffel symbols $\Gamma_{\alpha\beta}^\gamma = \boldsymbol{a}^\gamma \cdot \boldsymbol{a}_{\alpha,\beta}$. The external equivalent nodal forces are subdivided into components due to a constant body force $\boldsymbol{f}_0$, surface pressure q, boundary traction

t and boundary moment m_τ, that yield

$$\mathbf{f}^e_{\text{ext}0} := \int_{\Omega^e_0} \mathbf{N}^T \boldsymbol{f}_0 \, dA,$$

$$\mathbf{f}^e_{\text{ext}q} := \int_{\Omega^e} \mathbf{N}^T q \boldsymbol{n} \, da,$$

$$\mathbf{f}^e_{\text{ext}t} := \int_{\partial_t \Omega^e} \mathbf{N}^T \boldsymbol{t} \, ds,$$

$$\mathbf{f}^e_{\text{ext}m} := \int_{\partial_m \Omega^e} \mathbf{N}^T_{,\alpha} \nu^\alpha m_\tau \boldsymbol{n} \, ds.$$

(64)

The linearizations of δW^e_{int} and δW^e_{ext} are given in [37]. Similarly, inserting the above-mentioned interpolations into the weak form shown by Eq. (46), we obtain the fully discretized form of the balance of heat from Eq. (45) as

$$\delta W_\theta = \delta \boldsymbol{\theta}^T_e \underbrace{(\mathbf{f}^e_\theta - \mathbf{f}^e_{\bar{q}} + \mathbf{f}^e_Q)}_{\mathbf{R}^e_\theta},$$

(65)

where the thermal force vector $\mathbf{f}^e_\theta$, the boundary heat flux vector $\mathbf{f}^e_{\bar{q}}$ and the heat source vector $\mathbf{f}^e_Q$ are given by

$$\mathbf{f}^e_\theta = \int_{\Omega^e_0} k J (\boldsymbol{A}^\alpha \, \mathbf{N}^\star_{,\alpha})^T \cdot \boldsymbol{C}^{-1} \cdot \boldsymbol{A}^\alpha \, \mathbf{N}^\star_{,\alpha} \, \boldsymbol{\theta}_e \, dA,$$

$$\mathbf{f}^e_{\bar{q}} = \int_{\partial_q \Omega^e} \mathbf{N}^{\star T} \bar{q} \, ds,$$

$$\mathbf{f}^e_Q = \int_{\Omega^e} \mathbf{N}^{\star T} Q \, dA.$$

(66)

The nodal energy residual $\mathbf{R}^e_\theta$ can then be expressed as

$$\mathbf{R}^e_\theta = \int_{\Omega^e_0} k \, J \, (\boldsymbol{A}^\alpha \, \mathbf{N}^\star_{,\alpha})^T \cdot \boldsymbol{C}^{-1} \cdot \, \boldsymbol{A}^\alpha \, \mathbf{N}^\star_{,\alpha} \, \boldsymbol{\theta}_e \, dA - \int_{\partial_q \Omega^e} \mathbf{N}^{\star T} \bar{q} \, ds + \int_{\Omega^e} \mathbf{N}^{\star T} Q \, dA.$$

(67)

4.3. Lagrange multiplier method for rotational constraints

For the multipatch shell structures examined in the numerical examples, C^1-continuity at patch interfaces is required. To enforce this rotational constraint, we introduce the constraint potential

$$W_g = \int_{\mathcal{L}_0} \lambda \, (\bar{g}_c + \bar{g}_s) \, dS,$$

(68)

in the shell formulation. Here the integration is performed on the reference surface, λ denotes the Lagrange multiplier and

$$\bar{g}_c := 1 - \cos(\zeta - \zeta_0),$$

(69)

$$\bar{g}_s := \sin(\zeta - \zeta_0),$$

(70)

with $\cos \zeta_0 := \boldsymbol{N} \cdot \bar{\boldsymbol{N}}$ and $\cos \zeta := \boldsymbol{n} \cdot \bar{\boldsymbol{n}}$. Here $\boldsymbol{N}$ and $\boldsymbol{n}$ are reference and spatial surface normal vectors for the patch considered while $\bar{\boldsymbol{N}}$ and $\bar{\boldsymbol{n}}$ are the counterparts for the neighboring patch. The variation, linearization and FE discretization of W_g are well detailed in [37].

5. Inverse analysis

An inverse analysis framework for the preceding coupled thermohyperelastic model is presented briefly here. Kinematic and hyperelastic constitutive nonlinearities are taken into account in this study. External stimuli, i.e. surface loads like out-of-plane pressure and heat sources, applied to produce a target shape for thin shell structures,

will be recovered. Inverse problems, where the solution is solved iteratively, can be expressed mathematically in the following form:

$$\text{minimize} \quad \mathcal{J}\Big(\mathbf{s}, \mathbf{u}(\mathbf{s}), \boldsymbol{\theta}(\mathbf{s})\Big)$$

$$h\Big(\mathbf{s}, \mathbf{u}(\mathbf{s}), \boldsymbol{\theta}(\mathbf{s})\Big) = 0 \tag{71}$$

$$\mathbf{s}_l \leq \mathbf{s} \leq \mathbf{s}_u,$$

where $\mathbf{s}$ denotes the design variables (i.e. a supplied heat source and a lateral pressure), $\mathbf{u}(\mathbf{s})$ and $\boldsymbol{\theta}(\mathbf{s})$ are the state variables (i.e. the nodal displacements and temperatures). In general, the objective function $\mathcal{J}$ is subjected to equality constraints h while the design variables $\mathbf{s}$ are restricted by the lower bound $\mathbf{s}_l$ and the upper bound $\mathbf{s}_u$, respectively. In this study, the design variables $\mathbf{s}$ can be identified based on the measured displacements and temperature at discrete points on the surface. A mapping of these variables to measurements is described by the forward operator as

$$F : X \rightarrow Y, \tag{72}$$

$$\mathbf{s} \mapsto \{\mathbf{u}, \boldsymbol{\theta}\}^T \tag{73}$$

in which X is a finite dimensional parameter space where a supplied heat source, external loads etc. are defined and Y is a finite dimensional measurement space. Based on measured quantities $\mathbf{u}^{meas}$ and $\boldsymbol{\theta}^{meas}$, determination of $\mathbf{s}$ via the inverse problem is conducted from the following equation

$$F(\mathbf{s}) = \begin{Bmatrix} \mathbf{u}^{meas} \\ \boldsymbol{\theta}^{meas} \end{Bmatrix}. \tag{74}$$

As the system in Eq. (74) may be ill-posed, we intend to solve the problem in the sense of a regularized least-squares solution, i.e. minimization of

$$\mathcal{J}(s, u(s)) = \frac{1}{2} \int_{\Omega} \left| \frac{u^{meas} - u(s)}{u_{max}(s)} \right|^2 d\Omega + \frac{1}{2} \int_{\Omega} \left| \frac{\theta^{meas} - \theta(s)}{\theta_{max}(s)} \right|^2 d\Omega + R(q), \tag{75}$$

where $u_{max}(s)$ and $\theta_{max}(s)$ are the respective maximum values of displacement and temperature fields; $R(q)$ is a regularization term [45]. The gradient-based method – moving asymptotes (MMA) [46] – is used to solve the objective function iteratively. Furthermore, nonlinear softening deformations of the shell structure are also reconstructed where shape changes resulting from buckling are permitted. The FE-based discretization of the objective function is then given by

$$\mathcal{J} = \frac{1}{2} \left\| \frac{\mathbf{u}^{meas} - \mathbf{u}}{u_{max}} \right\|^2 + \frac{1}{2} \left\| \frac{\boldsymbol{\theta}^{meas} - \boldsymbol{\theta}}{\theta_{max}} \right\|^2 + \beta \left\| q - q^0 \right\|^2, \tag{76}$$

where $u_{\max}$ and $\theta_{\max}$ denote the maximum values of the numerical displacement and temperature, respectively; $\mathbf{u}^{meas}$ and $\boldsymbol{\theta}^{meas}$ are the respective displacements and temperatures measured on the target shape; q^0 is chosen as a priori estimate of q; β refers to the regularization parameter. The total sensitivity of the objective function $\mathcal{J}$ w.r.t. design variables s_i is estimated using the chain rule of differentiation as follows:

$$\frac{d\mathcal{J}}{ds_i} = \frac{\partial \mathcal{J}}{\partial s_i} + \frac{\partial \mathcal{J}}{\partial \boldsymbol{\theta}} \frac{\partial \boldsymbol{\theta}}{\partial s_i} + \frac{\partial \mathcal{J}}{\partial \mathbf{u}} \frac{\partial \mathbf{u}}{\partial s_i}. \tag{77}$$

5.1. Adjoint problem

The FE equilibrium equations for nonlinear mechanics are given in the form

$$\mathbf{r}(\mathbf{u}, \boldsymbol{\theta}, \mathbf{s}) = \mathbf{f}_{int}(\mathbf{u}, \boldsymbol{\theta}, \mathbf{s}) - \mathbf{f}_{ext}(\mathbf{u}, \mathbf{s}) = \mathbf{0}, \tag{78}$$

with $\mathbf{f}_{int}$ and $\mathbf{f}_{ext}$ being the internal and external equivalent nodal forces, respectively. Differentiating Eq. (78) w.r.t. the design variables $\mathbf{s}$ we obtain

$$\frac{d\mathbf{r}}{d\mathbf{s}_i} = \frac{\partial \mathbf{f}_{int}}{\partial \mathbf{s}_i} + \frac{\partial \mathbf{f}_{int}}{\partial \boldsymbol{\theta}} \frac{\partial \boldsymbol{\theta}}{\partial \mathbf{s}_i} + \frac{\partial \mathbf{f}_{int}}{\partial \mathbf{u}} \frac{\partial \mathbf{u}}{\partial \mathbf{s}_i} - \left(\frac{\partial \mathbf{f}_{ext}}{\partial \mathbf{s}_i} + \frac{\partial \mathbf{f}_{ext}}{\partial \mathbf{u}} \frac{\partial \mathbf{u}}{\partial \mathbf{s}_i} \right) = \mathbf{0}. \tag{79}$$

The FE equilibrium equations for heat conduction are given in the form,

$$\mathbf{K}_\theta \, \boldsymbol{\theta} = \mathbf{f}_Q. \tag{80}$$

where $\mathbf{K}_\theta$, $\boldsymbol{\theta}$ and $\mathbf{f}_Q$ denote the global conductivity matrix, vector of nodal temperatures and heat force vector, respectively, which are given by

$$\mathbf{K}_\theta = \mathbb{A}_{i=1}^{nel} \int_{\Omega_0^e} kJ \, \mathbf{N}_{,\alpha}^{\star T} \, (\mathbf{A}^\alpha)^T \cdot \mathbf{C}^{-1} \, \mathbf{A}^\alpha \, \mathbf{N}_{,\alpha}^\star \, dA,$$

$$\mathbf{f}_Q = \mathbb{A}_{i=1}^{nel} \int_{\Omega^e} \mathbf{N}^{\star T} \, Q \, dA. \tag{81}$$

where $\mathbb{A}_{i=1}^{nel}$ is assembly operator. Differentiating Eq. (80) w.r.t. the design variables we obtain

$$\mathbf{K}_\theta \frac{\partial \boldsymbol{\theta}}{\partial s_i} = \frac{d\mathbf{f}_Q}{ds_i} - \frac{d\mathbf{K}_\theta}{ds_i} \boldsymbol{\theta} \tag{82}$$

In order to avoid computing the derivatives $\partial \mathbf{u}/\partial s_i$ and $\partial \boldsymbol{\theta}/\partial s_i$ in Eq. (77) explicitly, the *adjoint method* is employed for performing the sensitivity analysis. The derivative of the equilibrium equations (79) and (82) is added into the derivative of the objective function in Eq. (77) through the Lagrange multiplier approach as proposed by [47]. We thus have

$$\frac{d\mathcal{J}}{ds_i} = \frac{\partial \mathcal{J}}{\partial s_i} + \frac{\partial \mathcal{J}}{\partial \boldsymbol{\theta}} \frac{\partial \boldsymbol{\theta}}{\partial s_i} + \frac{\partial \mathcal{J}}{\partial \mathbf{u}} \frac{\partial \mathbf{u}}{\partial s_i} + \boldsymbol{\lambda}_\theta^T \left(\frac{d\mathbf{f}_Q}{ds_i} - \frac{d\mathbf{K}_\theta}{ds_i} \boldsymbol{\theta} - \mathbf{K}_\theta \frac{\partial \boldsymbol{\theta}}{\partial s_i} \right)$$
$$+ \boldsymbol{\lambda}_m^T \left(\frac{\partial \mathbf{f}_{\text{int}}}{\partial s_i} - \frac{\partial \mathbf{f}_{\text{ext}}}{\partial s_i} + \left(\frac{\partial \mathbf{f}_{\text{int}}}{\partial \mathbf{u}} - \frac{\partial \mathbf{f}_{\text{ext}}}{\partial \mathbf{u}} \right) \frac{\partial \mathbf{u}}{\partial s_i} + \frac{\partial \mathbf{f}_{\text{int}}}{\partial \boldsymbol{\theta}} \frac{\partial \boldsymbol{\theta}}{\partial s_i} \right). \tag{83}$$

Rearranging Eq. (83), we have

$$\frac{d\mathcal{J}}{ds_i} = \frac{\partial \mathcal{J}}{\partial s_i} - \boldsymbol{\lambda}_\theta^T \left(\frac{d\mathbf{K}_\theta}{ds_i} \boldsymbol{\theta} - \frac{d\mathbf{f}_Q}{ds_i} \right) + \boldsymbol{\lambda}_m^T \left(\frac{\partial \mathbf{f}_{\text{int}}}{\partial s_i} - \frac{\partial \mathbf{f}_{\text{ext}}}{\partial s_i} \right)$$
$$+ \left(\frac{\partial \mathcal{J}}{\partial \boldsymbol{\theta}} - \boldsymbol{\lambda}_\theta^T \mathbf{K}_\theta + \boldsymbol{\lambda}_m^T \frac{\partial \mathbf{f}_{\text{int}}}{\partial s_i} \right) \frac{\partial \boldsymbol{\theta}}{\partial s_i} + \left[\frac{\partial \mathcal{J}}{\partial \mathbf{u}} + \boldsymbol{\lambda}_m^T \left(\frac{\partial \mathbf{f}_{\text{int}}}{\partial s_i} - \frac{\partial \mathbf{f}_{\text{ext}}}{\partial s_i} \right) \right] \frac{\partial \mathbf{u}}{\partial s_i} \tag{84}$$

Then, the coefficient terms associated with $\partial \boldsymbol{\theta}/\partial s_i$ and $\partial \mathbf{u}/\partial s_i$ are set to zero. Set $\mathbf{K}_m = \partial \mathbf{f}_{\text{int}}/\partial s_i - \partial \mathbf{f}_{\text{ext}}/\partial s_i$, the adjoint vectors $\boldsymbol{\lambda}_m$ and $\boldsymbol{\lambda}_\theta$ are solved from the following mechanical adjoint equation

$$\mathbf{K}_m \boldsymbol{\lambda}_m = \left(\frac{\partial \mathcal{J}}{\partial \mathbf{u}} \right)^T, \tag{85}$$

and the following thermal adjoint equation

$$\mathbf{K}_\theta \boldsymbol{\lambda}_\theta = \left(\frac{\partial \mathcal{J}}{\partial \boldsymbol{\theta}} \right)^T + \left(\frac{\partial \mathbf{f}_{\text{int}}}{\partial \boldsymbol{\theta}} \right)^T \boldsymbol{\lambda}_m. \tag{86}$$

Eq. (84) now becomes

$$\frac{d\mathcal{J}}{ds_i} = \frac{\partial \mathcal{J}}{\partial s_i} - \boldsymbol{\lambda}_\theta^T \left(\frac{d\mathbf{K}_\theta}{ds_i} \boldsymbol{\theta} - \frac{d\mathbf{f}_Q}{ds_i} \right) - \boldsymbol{\lambda}_m^T \left(\frac{\partial \mathbf{f}_{\text{int}}}{\partial s_i} - \frac{\partial \mathbf{f}_{\text{ext}}}{\partial s_i} \right). \tag{87}$$

Defining vectors $\mathbf{z}$ and $\boldsymbol{\psi}$ with components $z_i = \partial \mathcal{J}/\partial u_i$ and $\psi_i = \partial \mathcal{J}/\partial \theta_i$ and considering the Dirichlet and Neumann boundary conditions

$$z_i = u_i^{meas} - u_i \text{ on } \Omega, \tag{88}$$

$$\psi_i = \theta_i^{meas} - \theta_i \text{ on } \Omega. \tag{89}$$

Eqs. (85) and (86) can be solved for the adjoint vectors $\boldsymbol{\lambda}_m$, $\boldsymbol{\lambda}_\theta$ in a similar manner as Eqs. (78) and (80). In the following, analytical sensitivities are employed to obtain the derivatives of $\mathbf{f}_{\text{ext}}$ and $\mathbf{f}_Q$ w.r.t. the design variables $\mathbf{s}$.

5.2. Analytical sensitivities

Consider a shell structure subjected to a supplied heat source Q and lateral pressure q. Hence, the two design variables are $s_1 = Q$ and $s_2 = q$. The derivatives $\partial \mathbf{f}_Q^e / \partial s_1$ and $\partial \mathbf{f}_{\text{ext}}^e / \partial s_2$ are given by

$$\frac{\partial \mathbf{f}_Q^e}{\partial s_1} = \frac{\partial \mathbf{f}_Q^e}{\partial Q} = -\int_{\Omega^e} \mathbf{N}^{\star T} \, da, \tag{90}$$

and

$$\frac{\partial \mathbf{f}_{\text{ext}}^e}{\partial s_2} = \frac{\partial \mathbf{f}_{\text{ext}}^e}{\partial q} = -\int_{\Omega^e} \mathbf{N}^T \boldsymbol{n} \, da. \tag{91}$$

These derivatives are then inserted into Eq. (87) to obtain $d\mathcal{J}/ds_i$.

5.3. The L-curve criterion for the selection of the regularization parameter

In order to avoid an ill-posed problem, Tikhonov regularization along with a variant of the L-curve criterion is employed. A residual L-curve presented in [45], that shows a log–log plot of the residual norm over a regularized solution, is adopted to select a proper regularization parameter. Two flat regions on the curve result from under and over regularization, respectively. The optimal regularization parameter is indicated by the intersection of the two regions. It can be determined by finding the point with maximal curvature.

6. Numerical results

Inspired by the nature, where plants that undergo local swelling change their shape, various studies to shape morphing of hyperelastic thin membranes (or shells) have been performed [8,33]. In these studies, the shape changes of geometric composite membranes were fabricated via gradient-driven flow of polymer chains from high density regions to low density regions. In this section, the effect of swelling-induced large deformations on soft thin geometric composite shells is demonstrated. Swelling can be viewed as a thermal-like strain driven by the concentration gradient. The steady-state equation for the concentration (which is independent of the strain) is given by Eq. (22). Initially, the geometric composites are flat. They deform into curved 3D disks once a heat source is supplied. In other words, swelling is driven by the thermal (or concentration) gradient and leads to shape change.

The validation of the proposed method is based on experiment-like data used to mimic experimental measurements in practical application. At first, an FE analysis is performed for a given shell structure that is subject to external stimuli. A NURBS-based FE formulation is used for this [48]. This gives the nodal surface displacement $\mathbf{u}^{forw}$, from which the *experiment-like data* $\mathbf{u}^{meas} := \mathbf{u}^{forw}(1 + 0.01\gamma)$, with random number $\gamma \in [-1, 1]$, is obtained. The random noise added to $\mathbf{u}^{forw}$ expresses small disturbances as they could occur in reality measurements. Secondly, a gradient-based method using the analytical sensitivities is employed to minimize Eq. (76) based on the experiment-like data. Analytical sensitivities are used to estimate the element derivatives required in Eq. (87). The inverse problem is then solved iteratively until the corresponding structural shape is reconstructed. The convergence criterion $\epsilon_{obj.func.} = |\frac{\mathcal{J}^j - \mathcal{J}^{j-1}}{\mathcal{J}^0}| \leqslant 10^{-3}$, where j is the iteration number used to terminate the inverse algorithm.

Three numerical examples for geometrically nonlinear shells are examined. The thermohyperelastic constitutive law presented in Section 3.2 is used to describe nonlinear behavior of the shells. Furthermore, lateral disturbing pressure is employed to trigger buckling shape changes to mimic the effect of imperfections. Consequently, the accuracy of the inverse analysis will be evaluated. The first example considers the deflection of a geometric composite beam. The second example considers the dome-like deformation of a geometric composite disk. The third example considers the saddle-like deformation of a geometric composite disk. We assume that the temperature is uniformly distributed through the thickness and the temperature in the reference configuration is equal to 0. We denote the Young's modulus, Poisson's ratio, thermal expansion coefficient, and thermal conductivity by E, ν, α_θ and k, respectively.
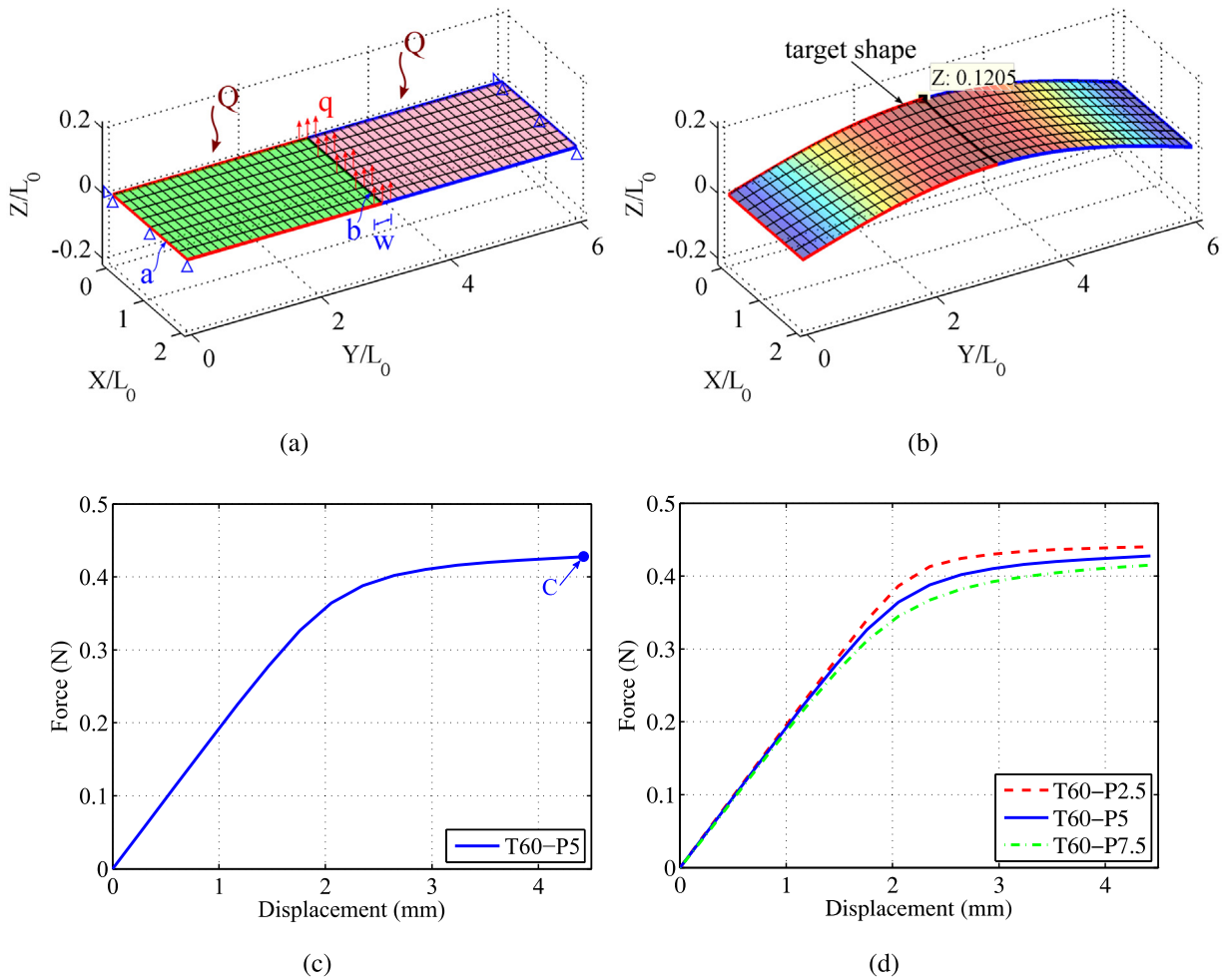
Fig. 3. Geometric composite beam subject to heat source Q and lateral disturbing pressure q: (a) undeformed shape, (b) deformed shape, (c) force–displacement curve, (d) effect of the lateral disturbing pressure q on the force–displacement curve. Here the legend, e.g. T60-P5, infers $Q = 60$ W/mm^2 and $q = 5 \times 10^{-3}$ N/mm^2.

6.1. Geometric composite beam subject to temperature change and lateral disturbing pressure

The first problem considers the buckling deformation of a geometric composite beam. The problem setup is shown in Fig. 3(a). A simply supported beam with dimensions $L \times W \times H = 2$ mm $\times 6$ mm $\times 0.2$ mm is subjected to an applied external heat source $Q = 60$ W/mm^2 and lateral disturbing pressure $q = 5 \times 10^{-3}$ N/mm^2 at mid-span. The beam is generated by two Bézier patches. A quadratic NURBS mesh with 8×48 elements is used here. The C^1-continuity at the interface between the two patches is enforced by the Lagrange multiplier method presented in Section 4.3 and [37]. The material properties are $E_1 = 1.2 \times 10^3$ N/mm^2, $\alpha_{\theta 1} = 10^{-4}$ K^{-1}, $k_1 = 10$ W/(mm K) for the left patch, and $E_2 = 10^3$ N/mm^2, $\alpha_{\theta 2} = 10^{-5}$ K^{-1}, $k_2 = 1$ W/(mm K) for the right patch. The incompressible Neo-Hookean model ($\nu = 0.5$) is used to describe both materials.

The heat source Q is supplied over the entire beam while the temperature $\bar{\theta} = 0$ is prescribed along the two pinned-end edges of the geometric composite beam. Under temperature change, the beam deforms as shown in Fig. 3(b). The sum of the reaction forces at the nodes on the left end (line a) versus the displacement at a point on the interface (line b) is plotted in Fig. 3(c). It is shown that the beam buckles when the reaction force at the pinned ends resulting from the thermal loading reaches approximately 0.4 N. Furthermore, the effect of the lateral disturbing pressure (i.e. load imperfection) on the force–displacement response is illustrated in Fig. 3(d). The target
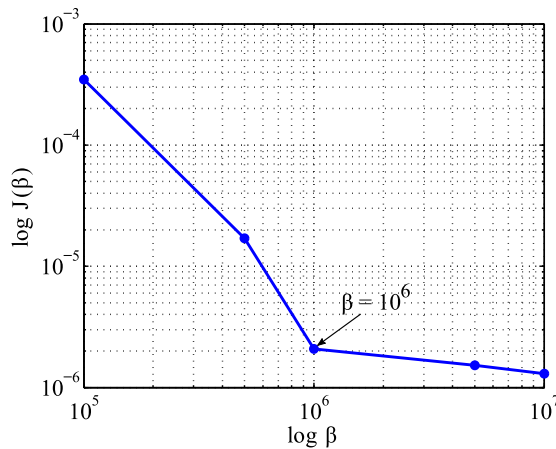
Fig. 4. Geometric composite beam subject to heat source Q and lateral disturbing pressure q. Residual L-curves corresponding to 1% noise: the objective function value over the regularization parameter β.

deformation corresponding to point C in Fig. 3(c). Experiment-like data is obtained by adding noise to this target deformation as mentioned above.

Inverse analysis based on the experiment-like data is then carried out. The residual L-curve, corresponding to data disturbed by 1% noise, is illustrated in Fig. 4. The curve is obtained through inverse analysis for regularization parameter β varied from 10^5 mm^2/N to 10^7 mm^2/N. The optimal regularization parameter β, indicated by the corner point on the curve, is approximately 10^6 mm^2/N. Convergence histories of the objective function and the L^2 error norm are illustrated in Fig. 5. The solution to the inverse problem, $Q^{inv} = 59.46$ W/mm^2 and $q^{inv} = 4.94 \times 10^{-3}$ N/mm^2, is obtained after 40 iterations. Overall, the proposed inverse method can accurately recover the applied heat source and the surface disturbing load as they are in good agreement with $Q^{meas} = 60$ W/mm^2 and $q^{meas} = 5 \times 10^{-3}$ N/mm^2. In addition, the corresponding shape, shown in Fig. 5(f), is reconstructed nearly identical to the target shape shown in Fig. 3(b). It should be noted that the target configuration is reconstructed in the presence of sudden shape changes.

In the following examples, we consider geometrically frustrated structures in form of flat disks. Those deform into dome-like and saddle-like shapes as a consequence of thermal expansion due to a surface heat source and different patterns of lateral disturbing pressure. It is worth noting that in this study the thermal expansion is analogous to (chemical) swelling as noted in the remark of Section 3.1.2. The analogous quantities to the heat source Q and the boundary heat flux $\bar{q}$ are then the adsorption S and the boundary mass flux $\bar{j}$.

6.2. Dome-shaped geometric composite disk

The second problem consists of a thermally induced swelling of a geometric composite disk. Geometrically, it is composed by an inner (pink) disk and an outer (green) annulus discretized with nine Bézier patches. We designed the geometry so that the outer annulus radii $R_i = 5$ mm and $R_e = 12$ mm is compatibly fitted to the inner disk with radius $r = 5$ mm, without pre-stretch. Both have thickness $h_d = h_a = 2$ mm. The problem geometry, boundary conditions and FE mesh are shown in Fig. 6(a). At the patch interfaces, C^1-continuity is enforced using the Lagrange multiplier method shown in Section 4.3. The edges along the circumferential direction of the disk shell are pinned. A thermohyperelastic incompressible material with $E_d = 12$ MPa, $E_a = 10$ MPa and $\nu_d = \nu_a = 0.5$ for the inner disk and the outer annulus, respectively, is used to model the material response. The thermal properties for the inner disk and the outer annulus are chosen respectively as $\alpha_{\theta d} = 5 \times 10^{-5}$ K^{-1}, $k_d = 5$ W/(mm K) and $\alpha_{\theta a} = 2 \times 10^{-5}$ K^{-1}, $k_a = 1$ W/(mm K).

The geometric composite disk is heated by the heat source $Q = 25$ W/mm^2 while keeping the surrounding temperature $\bar{\theta} = 0$ at the circumferential boundary $\partial_\theta S$ unchanged. The load imperfection depicted by the lateral disturbing pressure $q = 5 \times 10^{-3}$ N/mm^2 is applied on the inner disk, see Fig. 6(a). After deformation, the resultant dome-like shape can be observed in Fig. 6(b). Accordingly, the reaction force estimated at B versus the displacement
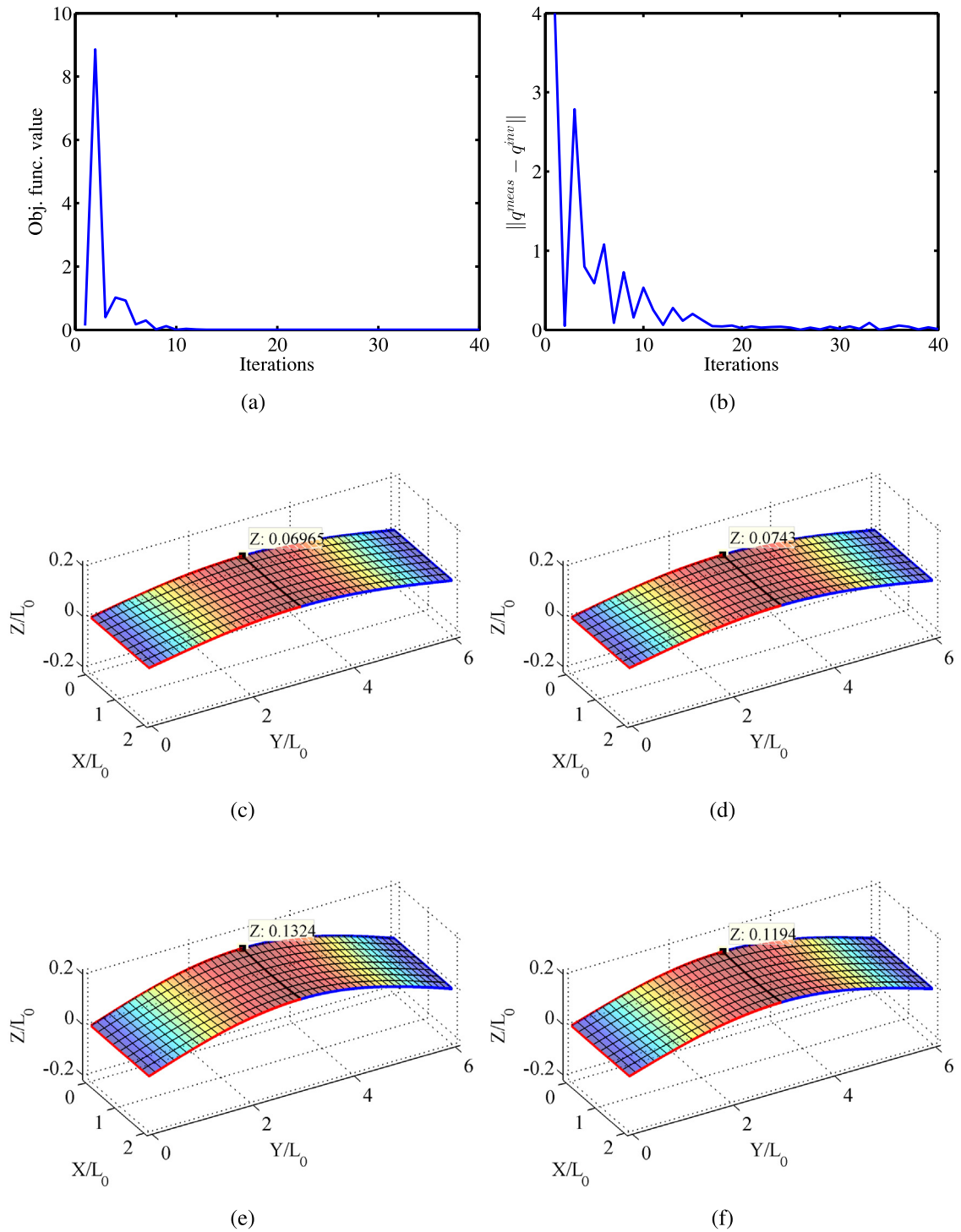
Fig. 5. Geometric composite beam subject to heat source and lateral disturbing pressure: (a) Convergence of the objective function, (b) L^2 error norm versus iteration number, (c) deformation at the initial iteration, (d) reconstructed deformation after 2 iterations, (e) reconstructed deformation after 4 iterations, (f) reconstructed deformation after 40 iterations.
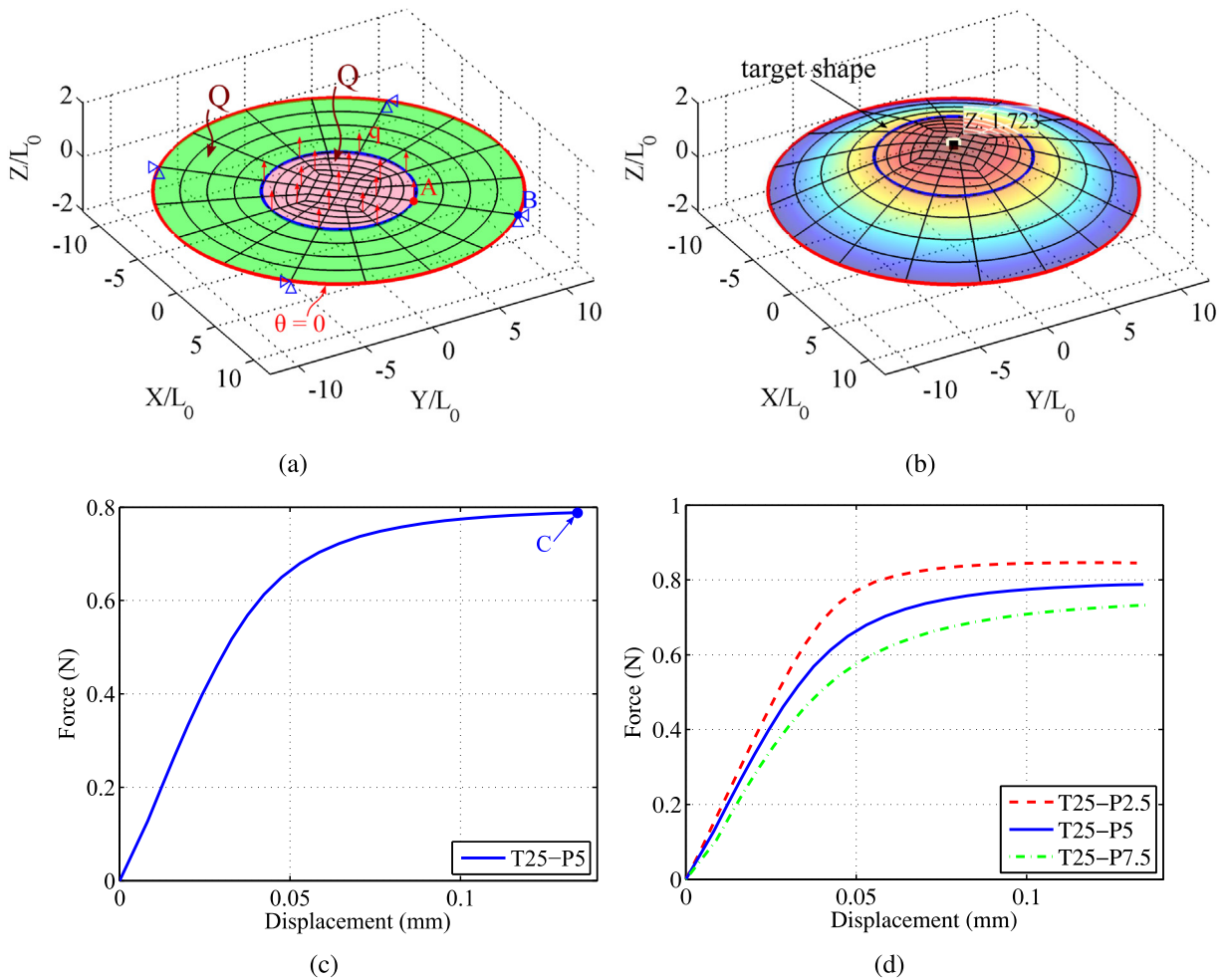
Fig. 6. Geometric composite disk subject to heat source Q and lateral disturbing pressure q: (a) undeformed shape, (b) deformed shape, (c) reaction force estimated at B versus displacement measured at A, (d) effect of the lateral disturbing pressure q on the force–displacement response. Here the legend, e.g. T25-P5, infers $Q = 25$ W/mm^2 and $q = 5 \times 10^{-3}$ N/mm^2. (For interpretation of the references to color in this figure legend, the reader is referred to the web version of this article.)

measured at A that shows the buckling behavior of the geometric composite disk is shown in Fig. 6(c). This plot shows that the disk softens with the reaction force at B being approximately 0.7 N. In addition, the effect of load imperfection on the force–displacement response is illustrated in Fig. 6(d). The experiment-like data, which is the nodal displacements of the deformed configuration shown in Fig. 6(b) along with additional noise, is then extracted to use for the inverse analysis. Note that the deformed shape corresponds to point C on the force–displacement curve plotted in Fig. 6(c).

Next, the prescribed heat source and lateral disturbing pressure are identified using the above obtained experiment-like data. The optimal regularization parameter $\beta \approx 10^8$ mm^2/N required by the Tikhonov regularization technique is chosen corresponding to the corner of the residual L-curve shown in Fig. 7. The convergence of the objective function and the convergence of L^2 error norm during the iteration are shown in Fig. 8. The inverse solution $Q^{inv} = 25.08$ W/mm^2 and $q^{inv} = 5.04 \times 10^{-3}$ N/mm achieved after 40 iterations is in good agreement with $Q^{meas} = 25$ W/mm^2 and $q^{meas} = 5 \times 10^{-3}$ N/mm. The accuracy of the inverse approach is highlighted in Fig. 8(f), which shows that the optimal shape is in excellent agreement with the target shape observed in Fig. 6(a). It is worth noting that the reconstruction of the target configuration is carried out while large shape changes (i.e. buckling) are allowed.
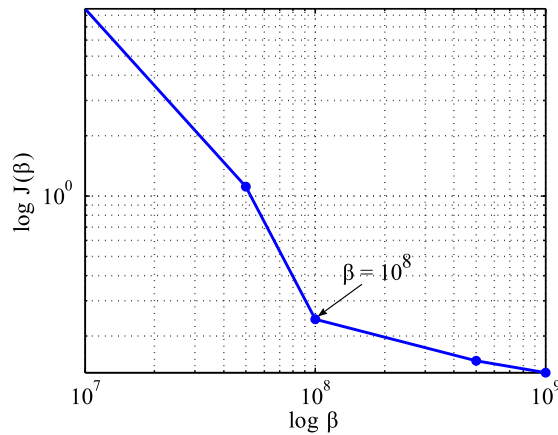
Fig. 7. Geometric composite disk subject to heat source Q and lateral disturbing pressure q. Residual L-curves corresponding to 1% noise: the objective function value over the regularization parameter β.

6.3. Saddle-shaped geometric composite disk

The third problem studies a saddle-shaped disk. We consider the problem setup given in Fig. 9(a). The geometric composite disk is modeled as an initially flat disk consisting of an inner pink disk and an outer green annulus. The radii of the inner disk ($r = 6$ mm) and the annulus ($R_i = 6$ mm and $R_e = 12$ mm) are ideally matched so that they are bonded without pre-stretch. The disk surface is clamped at the center and the outermost boundary is constrained in x and y directions as shown in Fig. 9(a). The center clamp is achieved by fixing the first ring of FE nodes around the center in z-direction as explained in [49].

A constant heat source $Q = 25$ W/mm^2 is prescribed over the entire structure. Zeros temperature is prescribed along the outermost boundary. Additionally, an altering lateral disturbing pressure is partially applied on the outer annulus as shown in Fig. 9(a). The disk is analyzed using 16×16 NURBS elements described by thermohyperelastic constitution using (1) the Koiter model and (2) the incompressible Neo-Hookean material model. At first, the Koiter model with $E_d = 1.2 \times 10^3$ MPa, $E_a = 10^3$ MPa and $\nu_d = \nu_a = 0.35$ for the inner disk and the outer annulus, respectively, is used. The lateral pressure whose magnitude $q = 0.1$ N/mm^2 is prescribed. The thermal properties are taken as $\alpha_{\theta d} = 2 \times 10^{-5}$ K^{-1}, $k_d = 5$ W/(mm K) and $\alpha_{\theta a} = 4 \times 10^{-5}$ K^{-1} and $k_a = 1$ W/(mm K). Under the stimuli, the resultant saddle-like shape of Fig. 9(b) can be observed. The reaction force at B versus the displacement at A is shown in Fig. 9(c).

Secondly, both bodies are described by the incompressible Neo-Hookean formulation with the material properties: $E_d = 12$ MPa, $E_a = 10$ MPa and $\nu_d = \nu_a = 0.5$. The thermal expansion coefficients $\alpha_{\theta d} = 2 \times 10^{-5}\,^{\circ}$C^{-1} and $\alpha_{\theta a} = 4 \times 10^{-5}\,^{\circ}$C^{-1} are taken. The lateral pressure whose magnitude is $q = 5 \times 10^{-3}$ N/mm^2 is applied. The deformed shape is shown in Fig. 10(a). Fig. 10(b) shows the reaction force at B versus the displacement measured at A.

Inverse analysis based on the nodal displacement of the target configuration shown in Fig. 9(b), is performed to recover the heat source Q and the lateral disturbing pressure q. Based on the residual L-curve described in Fig. 11, the optimal regularization parameter β is determined as 10^7 mm^2/N. Fig. 12 shows that the objective function and the L^2 error norm versus the number of iterations converge after 40 iterations. Good agreement between the inverse solutions $Q^{inv} = 24.94$ W/mm^2 and $q^{inv} = 0.1004$ N/mm^2 and $Q^{meas} = 25$ W/mm^2 and $q^{meas} = 0.1$ N/mm^2 is realized. Furthermore, the resulting structural deformation corresponding to the optimal solution, shown in Fig. 12(f), is nearly identical to the target shape. Likewise, for case (2) the deformed shape shown in Fig. 10(a) is adopted as experiment-like data. Inverse analysis is then carried out leading to the determination of heat source Q and lateral disturbing pressure q. The optimal regularization parameter $\beta \approx 5 \times 10^7$ mm^2/N corresponding to the corner point on the residual L-curve is taken, see Fig. 13. Reduction of the objective function and the L^2 error norm versus the iteration number are visualized in Fig. 14. The identified parameters $Q^{inv} = 24.89$ W/mm^2 and $q^{inv} = 7.484 \times 10^{-3}$ N/mm^2 are in good agreement with $Q^{meas} = 25$ W/mm^2 and $q^{meas} = 7.5 \times 10^{-3}$ N/mm^2. Accordingly, the target shape is accurately reconstructed after 40 iterations as shown in Fig. 14(f).
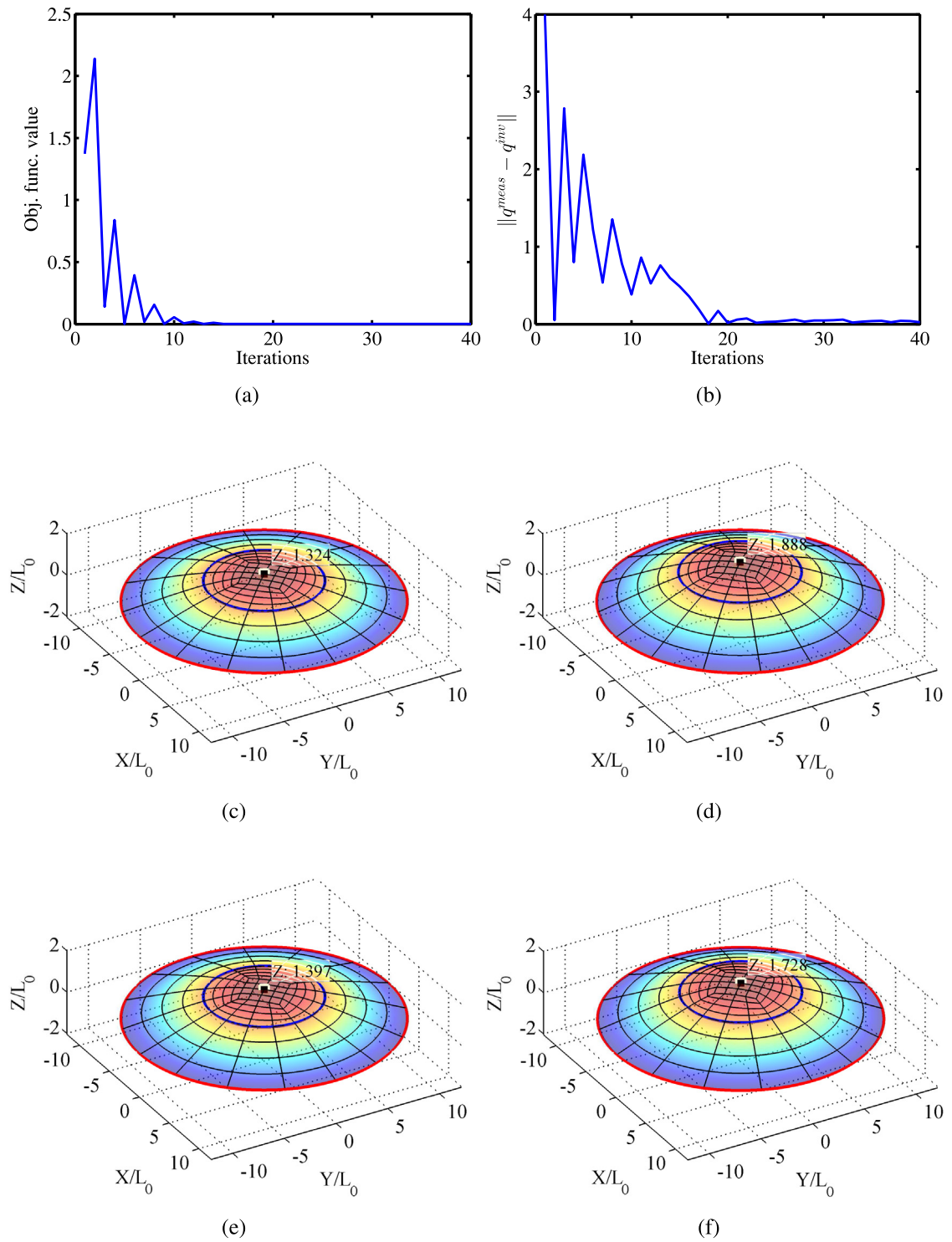
Fig. 8. Geometric composite disk subject to heat source Q and lateral disturbing pressure q: (a) Convergence of the objective function, (b) L^2 error norm versus iteration number, (c) deformation at the initial iteration, (d) reconstructed deformation at the first iteration, (e) reconstructed deformation after 2 iterations, (f) reconstructed deformation after 40 iterations.
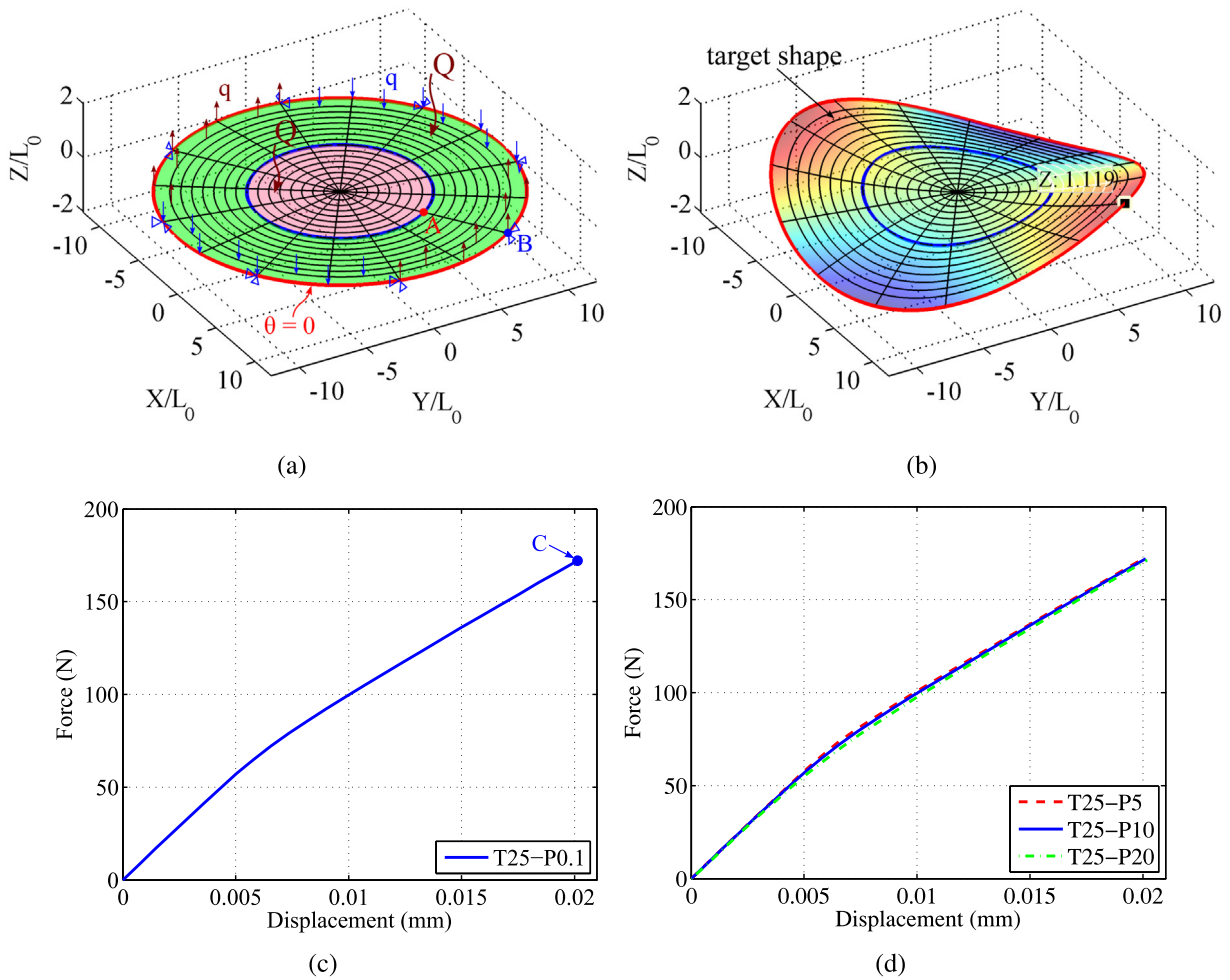
Fig. 9. Geometric composite disk subject to heat source Q and partially opposite lateral disturbing pressure q: (a) undeformed shape, (b) deformed shape, (c) reaction force estimated at B versus displacement measured at A, (d) effect of the lateral disturbing pressure q on the force–displacement response. Here the legend, e.g. T25-P0.1, infers $Q = 25$ W/mm^2 and $q = 0.1$ N/mm^2. (For interpretation of the references to color in this figure legend, the reader is referred to the web version of this article.)
Source: The thermohyperelastic theory using the Koiter model is formulated.

7. Conclusions

A new computational framework has been developed to study morphing of geometric composites from 2D thin sheets to nontrivial 3D shapes due to swelling-induced buckling. An inverse analysis was used to determine the external stimuli and reconstruct the corresponding shape within the framework of a nonlinear field theory. A gradient-based optimization method using analytical sensitivities was employed to tackle inverse problems. We have applied the proposed method to several examples motivated by practical applications in the field of soft matter. The nonlinear deformations can be reconstructed based on given experiment-like data. Especially, large shape changes can be captured accurately. We believe that this study provides an effective design tool for manufacturing of stimuli-responsive materials. It allows us to generate desired 3D shapes of geometric composites by appropriately prescribing external stimuli on thin flat sheets. The inverse analysis for the thermomechanics of layered composite shells for example considered in [50–53], where the shell deformation results from nonuniform heating and local swelling, can be studied in future work. Furthermore, this study can be extended to path-dependent materials straightforwardly. For example, one can model viscoelastic or elastoplastic shells based on a multiplicative decomposition of the surface deformation gradient [38].
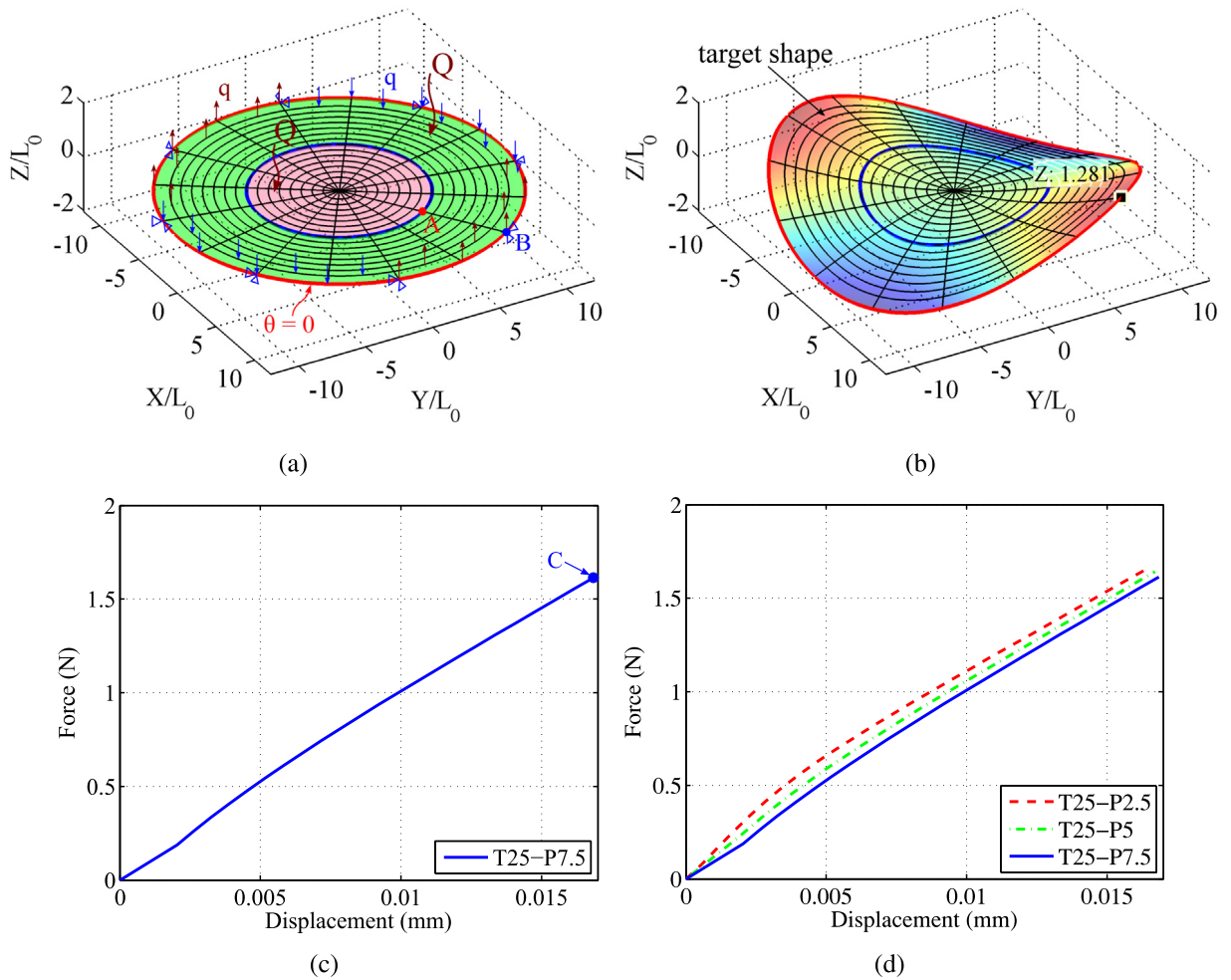
Fig. 10. Geometric composite disk subject to heat source Q and partially opposite lateral disturbing pressure q: (a) undeformed shape, (b) deformed shape, (c) reaction force estimated at B versus displacement measured at A, (d) effect of the lateral disturbing pressure q on the force–displacement response. Here the legend, e.g. T25-P0.1, infers $Q = 25$ W/mm^2 and $q = 5 \times 10^{-3}$ N/mm^2.
Source: The thermohyperelastic theory using the incompressible Neo-Hookean formulation is adopted.

Acknowledgments

Appendix A. Linearization of kinematical quantities in the direction Δx

A.1. Linearization of the surface stretch J in the direction Δx

The change of J shown in Eq. (12) in the direction $\Delta \mathbf{x}$ is given by [54] as follows

$$\Delta_x J = \frac{\partial J}{\partial \boldsymbol{a}_\alpha} \cdot \Delta_x \boldsymbol{a}_\alpha = J \boldsymbol{a}^\alpha \cdot \Delta_x \boldsymbol{a}_\alpha = J \boldsymbol{a}^\alpha \cdot \mathbf{N}_{,\alpha} \, \Delta \mathbf{x}_e. \tag{A.1}$$
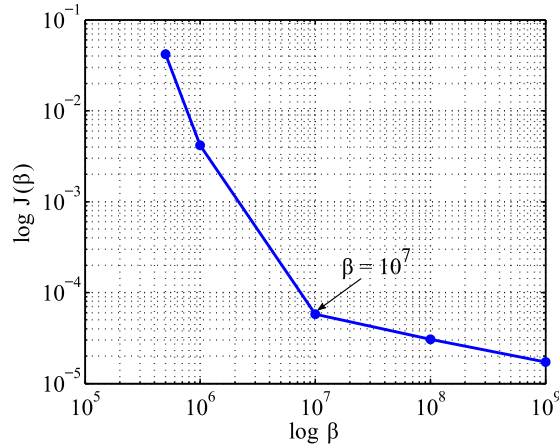
Fig. 11. Geometric composite disk subject to heat source Q and partially opposite lateral disturbing pressure q. Residual L-curves corresponding to 1% noise: the objective function value over the regularization parameter β.
Source: The thermohyperelastic theory using the Koiter model is formulated.

A.2. Linearization of C^{-1} in the direction Δx

Linearizing the inverse of the right Cauchy–Green strain C shown in Eq. (14) in the direction $\Delta \mathbf{x}$, we obtain

$$\Delta_x C^{-1} = \Delta_x a^{\alpha\beta} \; A_\alpha \otimes A_\beta \tag{A.2}$$

where the change of $a^{\alpha\beta}$ in the direction $\Delta \mathbf{x}$, referred from [41], can be written as

$$\Delta_x a^{\alpha\beta} = \frac{\partial a^{\alpha\beta}}{\partial a_{\gamma\delta}} \; \Delta_x a_{\gamma\delta} = a^{\alpha\beta\gamma\delta} \; \Delta_x a_{\gamma\delta} = a^{\alpha\beta\gamma\delta} \; a_\gamma \cdot \mathbf{N}_{,\delta} \; \Delta \mathbf{x}_e, \tag{A.3}$$

with

$$a^{\alpha\beta\gamma\delta} = -\frac{1}{2} \left(a^{\alpha\gamma} a^{\beta\delta} + a^{\alpha\delta} a^{\beta\gamma} \right), \tag{A.4}$$

Appendix B. Linearization of kinematical quantities in the direction $\Delta\theta$

B.1. Linearization of $\hat{\boldsymbol{a}}_\alpha$ and $\hat{\boldsymbol{a}}^\alpha$ in the direction $\Delta\theta$

According to Eq. ((55).1), we linearize $\hat{\boldsymbol{a}}_\alpha = \varphi \, A_\alpha$ and $\hat{\boldsymbol{a}}^\alpha = (1/\varphi) \, A^\alpha$ to give

$$\Delta_\theta \hat{\boldsymbol{a}}_\alpha = \alpha \; A_\alpha \; \mathbf{N}^\star \; \Delta\boldsymbol{\theta}_e \tag{B.1}$$

and

$$\Delta_\theta \hat{\boldsymbol{a}}^\alpha = -\frac{\alpha}{\varphi^2} \; A^\alpha \; \mathbf{N}^\star \; \Delta\boldsymbol{\theta}_e. \tag{B.2}$$

B.2. Linearization of $\hat{a}_{\alpha\beta}$ and $\hat{a}^{\alpha\beta}$ in the direction $\Delta\theta$

We linearize $\hat{a}_{\alpha\beta} = \hat{\boldsymbol{a}}_\alpha \cdot \hat{\boldsymbol{a}}_\beta$ and $\hat{a}^{\alpha\beta} = \hat{\boldsymbol{a}}^\alpha \cdot \hat{\boldsymbol{a}}^\beta$ in the direction $\Delta\theta$ to give

$$\begin{aligned}
\Delta_\theta \hat{a}_{\alpha\beta} &= \hat{\boldsymbol{a}}_\alpha \cdot \Delta_\theta \hat{\boldsymbol{a}}_\beta + \Delta_\theta \hat{\boldsymbol{a}}_\alpha \cdot \hat{\boldsymbol{a}}_\beta = 2\alpha\varphi \; A_{\alpha\beta} \; \mathbf{N}^\star \; \Delta\boldsymbol{\theta}_e, \\
\Delta_\theta \hat{a}^{\alpha\beta} &= \hat{a}^{\alpha\beta\gamma\delta} \; \Delta_\theta \hat{a}_{\gamma\delta} = -2\frac{\alpha}{\varphi^3} \; A^{\alpha\beta} \; \mathbf{N}^\star \; \Delta\boldsymbol{\theta}_e
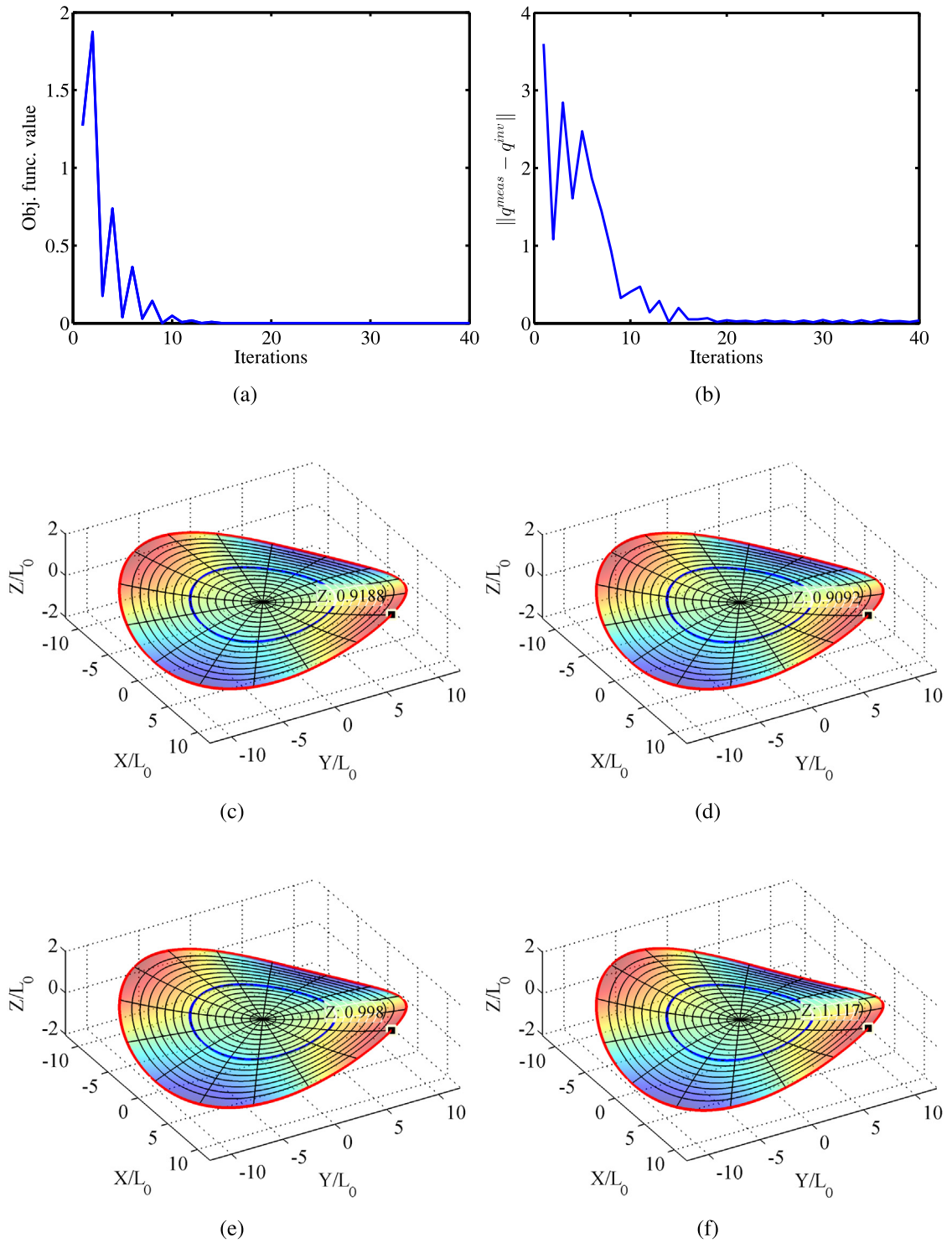\end{aligned} \tag{B.3}$$

Fig. 12. Geometric composite disk subject to heat source Q and partially opposite lateral disturbing pressure q: (a) Convergence of the objective function, (b) L^2 error norm versus iteration number, (c) deformation at the initial iteration, (d) reconstructed deformation after 2 iterations, (e) reconstructed deformation after 4 iterations, (f) reconstructed deformation after 40 iterations.
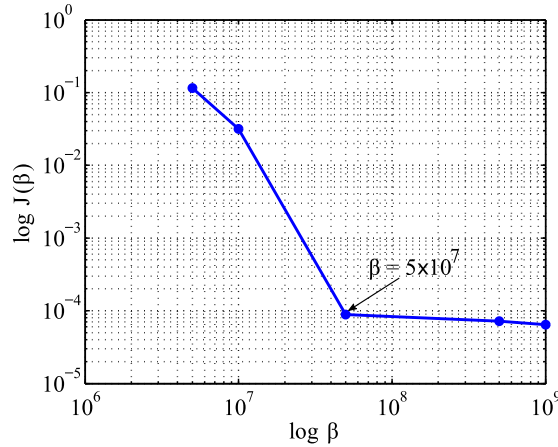*Source:* The thermohyperelastic theory using the Koiter model is formulated.

Fig. 13. Geometric composite disk subject to heat source Q and partially opposite lateral disturbing pressure q. Residual L-curves corresponding to 1% noise: the objective function value over the regularization parameter β.
Source: The thermohyperelastic theory using the incompressible Neo-Hookean formulation is adopted.

B.3. Linearization of $\hat{b}_{\alpha\beta}$ and $\hat{b}^{\alpha\beta}$ in the direction $\Delta\theta$

Linearizing $\hat{b}_{\alpha\beta} = \hat{\boldsymbol{n}} \cdot \hat{a}_{\alpha,\beta}$, $\tilde{\hat{b}}^{\alpha\beta} = 2\hat{H}\hat{a}^{\alpha\beta} - \hat{b}^{\alpha\beta}$ and $\kappa\hat{b}_{inv}^{\alpha\beta} = 2\hat{H}\hat{a}^{\alpha\beta} - \hat{b}^{\alpha\beta}$, we have

$$\Delta_\theta \hat{b}_{\alpha\beta} = \alpha \ B_{\alpha\beta} \ \mathbf{N}^\star \ \Delta\boldsymbol{\theta}_e \tag{B.4}$$

and

$$\begin{aligned}
\Delta_\theta \hat{b}^{\alpha\beta} &= \hat{b}^{\alpha\beta\gamma\delta} \ \Delta_\theta \hat{a}_{\gamma\delta} - \hat{a}^{\alpha\beta\gamma\delta} \ \Delta_\theta \hat{b}_{\gamma\delta} \\
&= \alpha \left(2\varphi \ \hat{b}^{\alpha\beta\gamma\delta} \ A_{\alpha\beta} - \hat{a}^{\alpha\beta\gamma\delta} \ B_{\alpha\beta} \right) \ \mathbf{N}^\star \ \Delta\boldsymbol{\theta}_e
\end{aligned} \tag{B.5}$$

with $a^{\alpha\beta\gamma\delta}$ being given in Eq. (A.4) and

$$\hat{b}^{\alpha\beta\gamma\delta} := -\frac{1}{2} \left(\hat{a}^{\alpha\gamma} \ \hat{b}^{\beta\delta} + \hat{b}^{\alpha\gamma} \ \hat{a}^{\beta\delta} + \hat{a}^{\alpha\delta} \ \hat{b}^{\beta\gamma} + \hat{b}^{\alpha\delta} \ \hat{a}^{\beta\gamma} \right). \tag{B.6}$$

B.4. Linearization of J_θ in the direction $\Delta\theta$

The linearization of J_θ, shown in Eq. (11), in the direction $\Delta\theta$ can be expressed by

$$\Delta_\theta J_\theta = 2\alpha\varphi \ \Delta\theta = 2\alpha\varphi \ \mathbf{N}^\star \ \Delta\boldsymbol{\theta}_e. \tag{B.7}$$

B.5. Linearization of $\hat{g}_{\alpha\beta}$ and $\hat{g}^{\alpha\beta}$ in the direction $\Delta\theta$

Linearizing $\hat{g}_{\alpha\beta}$ shown in Eq. ((34).1) in the direction $\Delta\theta$, we obtain

$$\Delta_\theta \hat{g}_{\alpha\beta} = \hat{g}_a \ \Delta_\theta \hat{a}_{\alpha\beta} + \hat{g}_b \ \Delta_\theta \hat{b}_{\alpha\beta} + \hat{a}_{\alpha\beta} \ \Delta_\theta \hat{g}_a + \hat{b}_{\alpha\beta} \ \Delta_\theta \hat{g}_b \tag{B.8}$$

with

$$\begin{aligned}
\Delta_\theta \hat{g}_a &= \xi^2 \hat{\kappa} \ \hat{a}^{\gamma\delta} \ \Delta_\theta \hat{a}_{\gamma\delta} - \xi^2 \ \tilde{\hat{b}}^{\gamma\delta} \ \Delta_\theta b_{\gamma\delta}, \\
\Delta_\theta \hat{g}_b &= -\xi^2 \ \hat{b}^{\gamma\delta} \ \Delta_\theta \hat{a}_{\gamma\delta} - \xi^2 \ \hat{a}^{\gamma\delta} \ \Delta_\theta b_{\gamma\delta}.
\end{aligned} \tag{B.9}$$

Similarly, the linearization of $\hat{g}^{\alpha\beta}$, shown in Eq. ((34).2), in the direction $\Delta\theta$ yields

$$\Delta_\theta \hat{g}^{\alpha\beta} = \hat{g}_a^{\alpha\beta\gamma\delta} \ \Delta_\theta \hat{a}_{\gamma\delta} + \hat{g}_b^{\alpha\beta\gamma\delta} \ \Delta_\theta \hat{b}_{\gamma\delta} \tag{B.10}$$
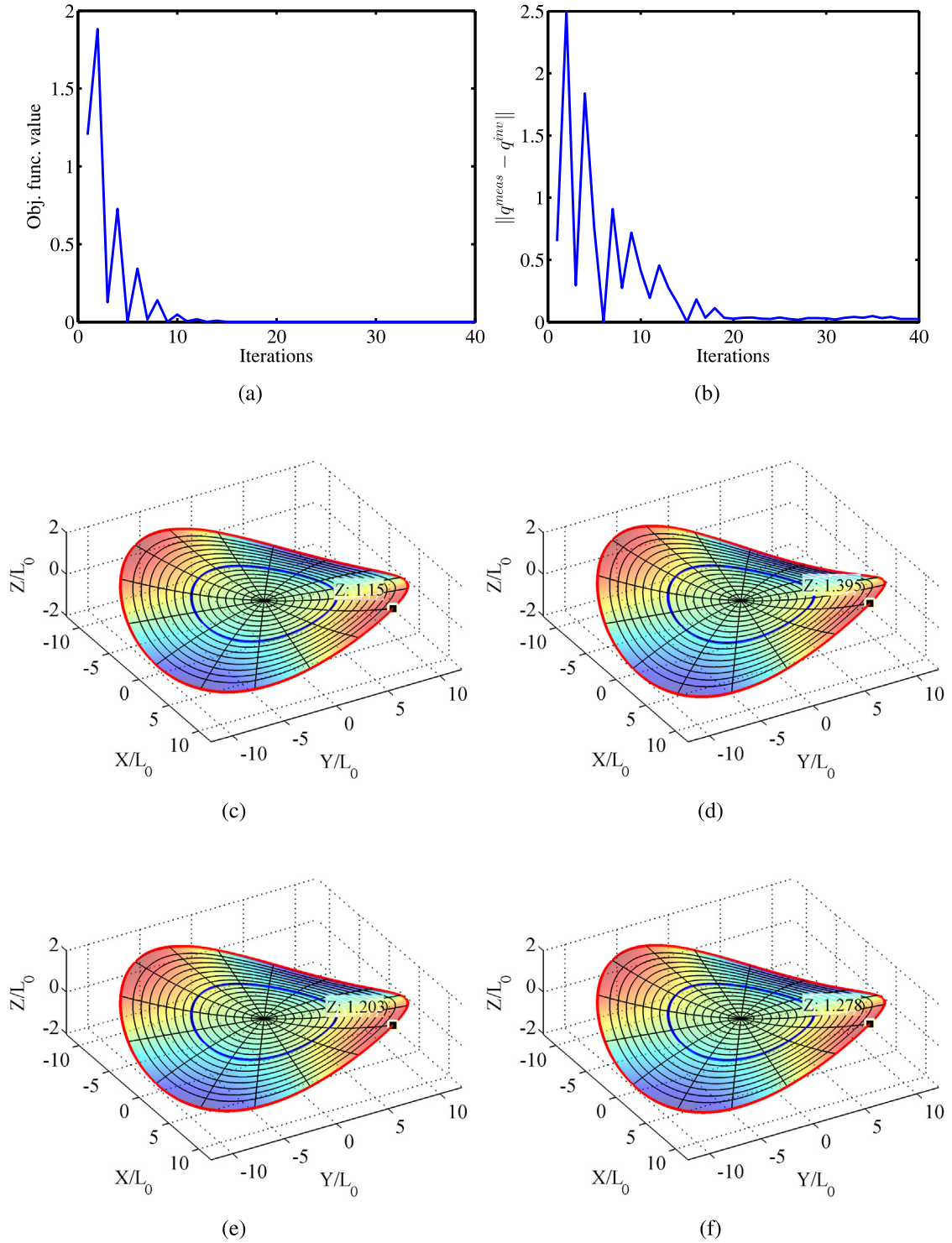
Fig. 14. Geometric composite disk subject to heat source Q and partially opposite lateral disturbing pressure q: (a) Convergence of the objective function, (b) L^2 error norm in parameter space X versus iteration number, (c) deformation at the initial iteration, (d) reconstructed deformation after 2 iterations, (e) reconstructed deformation after 4 iterations, (f) reconstructed deformation after 40 iterations. *Source:* The thermohyperelastic theory using the incompressible Neo-Hookean formulation is adopted.

where

$$\hat{g}_a^{\alpha\beta\gamma\delta} := \hat{s}^{-2} \left(\hat{a}^{\alpha\beta} \; \hat{\epsilon}_a^{\gamma\delta} + \hat{b}^{\alpha\beta} \; \hat{v}_a^{\gamma\delta} \right) + \hat{g}^a \; \hat{a}^{\alpha\beta\gamma\delta} + \hat{g}^b \; \hat{b}^{\alpha\beta\gamma\delta},$$

$$\hat{g}_b^{\alpha\beta\gamma\delta} := \hat{s}^{-2} \left(\hat{a}^{\alpha\beta} \; \hat{\epsilon}_b^{\gamma\delta} + \hat{b}^{\alpha\beta} \; \hat{v}_b^{\gamma\delta} \right) - \hat{g}^b \; \hat{a}^{\alpha\beta\gamma\delta}, \tag{B.11}$$

with

$$\hat{\epsilon}_a^{\alpha\beta} := \left(\hat{a}^{\alpha\beta} - \hat{g}^{-1} \; \hat{\mu}_a^{\alpha\beta} \right) \left(\hat{g}_a + 2\hat{H} \; \hat{g}_b \right) + \lambda_a^{\alpha\beta},$$

$$\hat{\epsilon}_b^{\alpha\beta} := -\hat{g}^{-1} \; \hat{\mu}_a^{\alpha\beta} \left(\hat{g}_a + 2\hat{H} \; \hat{g}_b \right) + \lambda_b^{\alpha\beta}. \tag{B.12}$$

and

$$\hat{v}_a^{\alpha\beta} := - \left(\hat{a}^{\alpha\beta} - \hat{g}^{-1} \; \hat{\mu}_a^{\alpha\beta} \right) \hat{g}_b - \xi^2 \; \hat{b}^{\alpha\beta},$$

$$\hat{v}_b^{\alpha\beta} := \hat{g}^{-1} \; \hat{\mu}_b^{\alpha\beta} \; \hat{g}_b - \xi^2 \; \hat{a}^{\alpha\beta}. \tag{B.13}$$

Here we defined

$$\hat{\lambda}_a^{\alpha\beta} := \xi^2 \hat{\kappa} \; \hat{a}^{\alpha\beta} - \left(2\hat{H}\xi^2 + \hat{g}_b \right) \hat{b}^{\alpha\beta},$$

$$\hat{\lambda}_b^{\alpha\beta} := \xi^2 \; \tilde{\hat{b}}^{\alpha\beta} + \left(2\hat{H}\xi^2 + \hat{g}_b \right) \hat{a}^{\alpha\beta}, \tag{B.14}$$

and

$$\hat{\mu}_a^{\alpha\beta} := 2\hat{a} \left(\hat{g}_a + \hat{H} \; \hat{g}_b \right) \xi^2 \hat{\kappa} \; \hat{a}^{\gamma\delta} - 2 \left(\hat{b} \; \hat{g}_b + \hat{H} \; \hat{a}\hat{g}_a \right) \xi^2 \; \hat{b}^{\gamma\delta} + \hat{g}_a^2 \; \hat{a} \; \hat{a}^{\gamma\delta} + \hat{g}_a \; \hat{g}_b \; \hat{a} \; \tilde{\hat{b}}^{\gamma\delta},$$

$$\hat{\mu}_b^{\alpha\beta} := -2\hat{a} \left(\hat{g}_a + \hat{H} \; \hat{g}_b \right) \xi^2 \; \tilde{\hat{b}}^{\gamma\delta} + 2 \left(\hat{b} \; \hat{g}_b + \hat{H} \; \hat{a}\hat{g}_a \right) \xi^2 \; \hat{a}^{\gamma\delta} + \hat{g}_b^2 \; \hat{a} \; \tilde{\hat{b}}^{\gamma\delta} + \hat{g}_a \; \hat{g}_b \; \hat{a} \; \hat{a}^{\gamma\delta}. \tag{B.15}$$

B.6. Linearization of $J_M^\star$ in the direction $\Delta\theta$

According to [37], the change

$$\Delta_\theta J_M^\star = \frac{J_M^\star}{2} \left(\hat{\omega}_a^{\alpha\beta} \; \Delta_\theta \hat{a}_{\alpha\beta} + \hat{\omega}_b^{\alpha\beta} \; \Delta_\theta \hat{b}_{\alpha\beta} \right) \tag{B.16}$$

is derived, where

$$\hat{\omega}_a^{\alpha\beta} := \xi^2 \; \hat{\kappa} \; \hat{m}_a \; \hat{a}^{\alpha\beta} - \xi^2 \; \hat{m}_b \; \hat{b}^{\alpha\beta} + \hat{g}_a \; \hat{g}^{\alpha\beta},$$

$$\hat{\omega}_b^{\alpha\beta} := -\xi^2 \; \hat{m}_a \; \tilde{\hat{b}}^{\alpha\beta} + \xi^2 \; \hat{m}_b \; \hat{a}^{\alpha\beta} + \hat{g}_b \; \hat{g}^{\alpha\beta}. \tag{B.17}$$

with $\hat{m}_a = \hat{g}^{\gamma\delta} \hat{a}_{\gamma\delta}$ and $\hat{m}_b = \hat{g}^{\gamma\delta} \hat{b}_{\gamma\delta}$.

B.7. Linearization $\hat{s}$ in the direction $\Delta\theta$

From Eq. (36), the change of $\hat{s}$ is described by

$$\Delta_\theta \hat{s} = 2\xi \; \Delta_\theta \hat{H} + \xi^2 \; \Delta_\theta \hat{\kappa}. \tag{B.18}$$

in which the mean curvature and the Gauss curvature associated with the thermal intermediate configuration $\hat{\mathcal{S}}$ are given by

$$\hat{H} = \frac{1}{2} \hat{a}^{\alpha\beta} \; \hat{b}_{\alpha\beta}, \quad \hat{\kappa} = \frac{\det[\hat{b}_{\alpha\beta}]}{\det[\hat{a}_{\alpha\beta}]} = \frac{\hat{b}}{\hat{a}}. \tag{B.19}$$

and the change of $\hat{H}$ and $\hat{\kappa}$ in the direction $\Delta\theta$ can thus be expressed as

$$\Delta_\theta \hat{H} = \frac{\partial \hat{H}}{\partial \hat{a}_{\alpha\beta}} \; \Delta_\theta \hat{a}_{\alpha\beta} + \frac{\partial \hat{H}}{\partial \hat{b}_{\alpha\beta}} \; \Delta_\theta \hat{b}_{\alpha\beta}$$

$$\Delta_\theta \hat{\kappa} = \frac{\partial \hat{\kappa}}{\partial \hat{a}_{\alpha\beta}} \; \Delta_\theta \hat{a}_{\alpha\beta} + \frac{\partial \hat{\kappa}}{\partial \hat{b}_{\alpha\beta}} \; \Delta_\theta \hat{b}_{\alpha\beta}, \tag{B.20}$$

with

$$\frac{\partial \hat{H}}{\partial \hat{a}_{\alpha\beta}} = -\frac{1}{2}\hat{b}^{\alpha\beta}, \qquad \frac{\partial \hat{H}}{\partial \hat{b}_{\alpha\beta}} = \frac{1}{2}\hat{a}^{\alpha\beta}$$

$$\frac{\partial \hat{\kappa}}{\partial \hat{a}_{\alpha\beta}} = -\kappa\hat{a}^{\alpha\beta}, \qquad \frac{\partial \hat{\kappa}}{\partial \hat{b}_{\alpha\beta}} = \kappa\hat{b}^{\alpha\beta}_{inv} = \tilde{\hat{b}}^{\alpha\beta}. \tag{B.21}$$

B.8. Linearization of $\tau_M^{\alpha\beta}$ and $M_M^{\alpha\beta}$ in the direction $\Delta\theta$

B.8.1. Koiter material model

Given by Eq. (37), the linearization of $\tau_M^{\alpha\beta}$ and $M_M^{\alpha\beta}$ can be expressed by

$$\Delta_\theta \tau_M^{\alpha\beta} = \left[-\frac{2\alpha}{\varphi^3} \left(\Lambda\, A^{\alpha\beta}\, \hat{a}^{\gamma\delta} + 2\mu\, A^{\alpha\gamma}\, \hat{a}^{\beta\delta} \right) \left(a_{\gamma\delta} - \hat{a}_{\gamma\delta} \right) - \alpha\varphi\, \hat{c}^{\alpha\beta\gamma\delta}\, A_{\gamma\delta} \right] \mathbf{N}^\star \Delta\boldsymbol{\theta}_e,$$

$$\Delta_\theta M_M^{\alpha\beta} = \left[-\frac{4\alpha}{\varphi^3} \frac{T^2}{12} \left(\Lambda\, A^{\alpha\beta}\, \hat{a}^{\gamma\delta} + 2\mu\, A^{\alpha\gamma}\, \hat{a}^{\beta\delta} \right) \left(b_{\gamma\delta} - \hat{b}_{\gamma\delta} \right) - \alpha\, \hat{f}^{\alpha\beta\gamma\delta}\, B_{\gamma\delta} \right] \mathbf{N}^\star \Delta\boldsymbol{\theta}_e. \tag{B.22}$$

where $\hat{c}^{\alpha\beta\gamma\delta}$ and $\hat{f}^{\alpha\beta\gamma\delta}$ are given by Eq. (31).

B.8.2. Incompressible Neo-Hookean material model

According to Eq. (37), we can derive the following linearizations

$$\Delta_\theta \tau_M^{\alpha\beta} = \int_{-\frac{T}{2}}^{\frac{T}{2}} \left[\Delta_\theta \hat{s} \left(1 - \xi^2\kappa \right) \tilde{\tau}_M^{\alpha\beta} + \hat{s} \left(1 - \xi^2\kappa \right) \Delta_\theta \tilde{\tau}_M^{\alpha\beta} \right] d\xi,$$

$$\Delta_\theta M_M^{\alpha\beta} = \int_{-\frac{T}{2}}^{\frac{T}{2}} \left[\Delta_\theta \hat{s} \left(-\xi + \xi^2 H \right) \tilde{\tau}_M^{\alpha\beta} + \hat{s} \left(-\xi + \xi^2 H \right) \Delta_\theta \tilde{\tau}_M^{\alpha\beta} \right] d\xi, \tag{B.23}$$

where $\tilde{\tau}_M^{\alpha\beta}$ is given by Eq. (40), we can thus derive the following linearization

$$\Delta_\theta \tilde{\tau}_M^{\alpha\beta} = \tilde{\mu} \left(\Delta_\theta \hat{g}^{\alpha\beta} + 2\frac{\Delta_\theta J_M^\star}{J_M^{\star^3}} g^{\alpha\beta} \right), \tag{B.24}$$

with $\Delta_\theta \hat{g}^{\alpha\beta}$ and $\Delta_\theta J_M^\star$ being given in Eqs. (B.10) and (B.16), respectively, we obtain

$$\Delta_\theta \tilde{\tau}_M^{\alpha\beta} = \tilde{\mu}\, \alpha \left[\left(2\varphi\, A_{\gamma\delta}\, \hat{g}_a^{\alpha\beta\gamma\delta} + B_{\gamma\delta}\, \hat{g}_b^{\alpha\beta\gamma\delta} \right) + \frac{1}{J_M^{\star^2}} \left(2\varphi\, A_{\alpha\beta}\, \hat{\omega}_a^{\alpha\beta} + B_{\alpha\beta}\, \hat{\omega}_b^{\alpha\beta} \right) \right] \mathbf{N}^\star \Delta\boldsymbol{\theta}_e. \tag{B.25}$$

References

[1] M.A.C. Stuart, W.T. Huck, J. Genzer, M. Müller, C. Ober, M. Stamm, G.B. Sukhorukov, I. Szleifer, V.V. Tsukruk, M. Urban, F. Winnik, Emerging applications of stimuli-responsive polymer materials, Nat. Mater. 9 (2) (2010) 101.

[2] L. Ionov, Soft microorigami: Self-folding polymer films, Soft Matter 7 (15) (2011) 6786–6791.

[3] Y. Forterre, J.M. Skotheim, J. Dumais, L. Mahadevan, How the Venus flytrap snaps, Nature 433 (7024) (2005) 421.

[4] N.C. Heer, P.W. Miller, S. Chanet, N. Stoop, J. Dunkel, A.C. Martin, Actomyosin-based tissue folding requires a multicellular myosin gradient. development, dev-146761, 2017.

[5] M. Pezzulla, N. Stoop, M.P. Steranka, A.J. Bade, D.P. Holmes, Curvature-induced instabilities of shells, Phys. Rev. Lett. 120 (4) (2018) 048002.

[6] E. Katifori, S. Alben, E. Cerda, D.R. Nelson, J. Dumais, Foldable structures and the natural design of pollen grains, Proc. Natl. Acad. Sci. 107 (17) (2010) 7635–7639.

[7] H.W.G. Lim, M. Wortis, R. Mukhopadhyay, Stomatocyte–discocyte–echinocyte sequence of the human red blood cell: Evidence for the bilayer–couple hypothesis from membrane mechanics, Proc. Natl. Acad. Sci. 99 (26) (2002) 16766–16769.

[8] M. Pezzulla, S.A. Shillig, P. Nardinocchi, D.P. Holmes, Morphing of geometric composites via residual swelling, Soft Matter 11 (29) (2015) 5812–5820.

[9] Y. Klein, E. Efrati, E. Sharon, Shaping of elastic sheets by prescription of non-Euclidean metrics, Science 315 (5815) (2007) 1116–1120.

[10] M. Pezzulla, N. Stoop, X. Jiang, D.P. Holmes, Curvature-driven morphing of non-Euclidean shells, Proc. R. Soc. Lond. Ser. A Math. Phys. Eng. Sci. 473 (2201) (2017) 20170087.

[11] J. Kim, J.A. Hanna, M. Byun, C.D. Santangelo, R.C. Hayward, Designing responsive buckled surfaces by halftone gel lithography, Science 335 (2012) 1201–1205.
[12] M. Pezzulla, G.P. Smith, P. Nardinocchi, D.P. Holmes, Geometry and mechanics of thin growing bilayers, Soft Matter 12 (19) (2016) 4435–4442.
[13] T. Mora, A. Boudaoud, Buckling of swelling gels, Eur. Phys. J. E 20 (2) (2006) 119–124.
[14] J.A. Gemmer, S.C. Venkataramani, Shape selection in non-Euclidean plates, Physica D 240 (19) (2011) 1536–1552.
[15] J. Kim, J.A. Hanna, R.C. Hayward, C.D. Santangelo, Thermally responsive rolling of thin gel strips with discrete variations in swelling, Soft Matter 8 (8) (2012) 2375–2381.
[16] E. Efrati, E. Sharon, R. Kupferman, Elastic theory of unconstrained non-Euclidean plates, J. Mech. Phys. Solids 57 (4) (2009) 762–775.
[17] J. Kiendl, K.U. Bletzinger, J. Linhard, R. Wüchner, Isogeometric shell analysis with Kirchhoff–Love elements, Comput. Methods Appl. Mech. Engrg. 198 (49–52) (2009) 3902–3914.
[18] D.J. Benson, Y. Bazilevs, M.C. Hsu, T.J.R. Hughes, Isogeometric shell analysis: the Reissner–Mindlin shell, Comput. Methods Appl. Mech. Engrg. 199 (5–8) (2010) 276–289.
[19] W.A. Wall, M.A. Frenzel, C. Cyron, Isogeometric structural shape optimization, Comput. Methods Appl. Mech. Engrg. 197 (33–40) (2008) 2976–2988.
[20] J. Kiendl, R. Schmidt, R. Wüchner, K.U. Bletzinger, Isogeometric shape optimization of shells using semi-analytical sensitivity analysis and sensitivity weighting, Comput. Methods Appl. Mech. Engrg. 274 (2014) 148–167.
[21] Y.D. Seo, H.J. Kim, S.K. Youn, Shape optimization and its extension to topological design based on isogeometric analysis, Int. J. Solids Struct. 47 (11–12) (2010) 1618–1640.
[22] H. Ghasemi, H.S. Park, T. Rabczuk, A level-set based IGA formulation for topology optimization of flexoelectric materials, Comput. Methods Appl. Mech. Engrg. 313 (2017) 239–258.
[23] M. Bischoff, E. Ramm, J. Irslinger, Models and finite elements for thin-walled structures, Encyclopedia of Computational Mechanics, Second ed., 2018, pp. 1–86.
[24] P.R. Budarapu, J. Reinoso, M. Paggi, Concurrently coupled solid shell-based adaptive multiscale method for fracture, Comput. Methods Appl. Mech. Engrg. 319 (2017) 338–365.
[25] Y. Bazilevs, M.S. Pigazzini, A. Ellison, H. Kim, A new multi-layer approach for progressive damage simulation in composite laminates based on isogeometric analysis and Kirchhoff? Love shells. Part I: Basic theory and modeling of delamination and transverse shear, Comput. Mech. 62 (3) (2018) 563–585.
[26] R. Echter, M. Bischoff, Numerical efficiency, locking and unlocking of NURBS finite elements, Comput. Methods Appl. Mech. Engrg. 199 (5–8) (2010) 374–382.
[27] R. Echter, B. Oesterle, M. Bischoff, A hierarchic family of isogeometric shell finite elements, Comput. Methods Appl. Mech. Engrg. 254 (2013) 170–180.
[28] L. Leonetti, F. Liguori, D. Magisano, G. Garcea, An efficient isogeometric solid-shell formulation for geometrically nonlinear analysis of elastic shells, Comput. Methods Appl. Mech. Engrg. 331 (2018) 159–183.
[29] M. Doi, Gel dynamics, J. Phys. Soc. Japan 78 (5) (2009) 052001–052001.
[30] S.A. Chester, L.A. Di Leo, Finite element implementation of a coupled diffusion-deformation theory for elastomeric gels, Int. J. Solids Struct. 52 (2015) 1–18.
[31] T. Tanaka, D.J. Fillmore, Kinetics of swelling of gels, J. Chem. Phys. 70 (3) (1979) 1214–1218.
[32] S.A. Chester, L. Anand, A thermo-mechanically coupled theory for fluid permeation in elastomeric materials: Application to thermally responsive gels, J. Mech. Phys. Solids 59 (10) (2011) 1978–2006.
[33] A. Lucantonio, L. Teresi, A. DeSimone, Continuum theory of swelling material surfaces with applications to thermo-responsive gel membranes and surface mass transport, J. Mech. Phys. Solids 89 (2016) 96–109.
[34] M.B. Amar, A. Goriely, Growth and instability in elastic tissues, J. Mech. Phys. Solids 53 (10) (2005) 2284–2319.
[35] P.M. Naghdi, The theory of shells and plates, in: Flugge's Handbuch der Physik, vol. VI a/C, Truesdell, 1972.
[36] D.J. Steigmann, On the relationship between the Cosserat and Kirchhoff–Love theories of elastic shells, Math. Mech. Solids 4 (3) (1999) 275–288.
[37] T.X. Duong, F. Roohbakhshan, R.A. Sauer, A new rotation-free isogeometric thin shell formulation and a corresponding continuity constraint for patch boundaries, Comput. Methods Appl. Mech. Engrg. 316 (2017) 43–83.
[38] R.A. Sauer, R. Ghaffari, A. Gupta, The multiplicative deformation split for shells with application to growth, chemical swelling, thermoelasticity, viscoelasticity and elastoplasticity, 2018, arXiv preprint arXiv:1810.10384.
[39] G. Holzapfel, Nonlinear Solid Mechanics: A Continuum Approach for Engineering, John Wiley & Sons, Ltd., West Sussex, England, 2000.
[40] A. Sahu, R.A. Sauer, K.K. Mandadapu, Irreversible thermodynamics of curved lipid membranes, Phys. Rev. E 96 (4) (2017) 042409.
[41] R.A. Sauer, T.X. Duong, On the theoretical foundations of thin solid and liquid shells, Math. Mech. Solids 22 (3) (2015) 343–371.
[42] N. Vu-Bac, T.X. Duong, T. Lahmer, X. Zhuang, R.A. Sauer, H.S. Park, T. Rabczuk, A NURBS-based inverse analysis for reconstruction of nonlinear deformations of thin shell structures, Comput. Methods Appl. Mech. Engrg. 331 (2018) 427–455.
[43] M.J. Borden, M.A. Scott, J.A. Evans, T.J.R. Hughes, Isogeometric finite element data structures based on Bezier extraction of NURBS, Internat. J. Numer. Methods Engrg. 87 (1–5) (2011) 15–47.
[44] R.A. Sauer, On the computational modeling of lipid bilayers using thin-shell theory, in: In the Role of Mechanics in the Study of Lipid Bilayers, Springer, Cham, 2018, pp. 221–286.
[45] S.S. Nanthakumar, T. Lahmer, X. Zhuang, G. Zi, T. Rabczuk, Detection of material interfaces using a regularized level set method in piezoelectric structures, Inverse Probl. Sci. Eng. 24 (1) (2016) 153–176.

[46] K. Svanberg, The method of moving asymptotes - a new method for structural optimization, Internat. J. Numer. Methods Engrg. 24 (2) (1987) 359–373.

[47] R.T. Haftka, Z. Gürdal, Elements of Structural Optimization, Springer Science & Business Media, 2012.

[48] T.J.R. Hughes, J.A. Cottrell, Y. Bazilevs, Isogeometric analysis: CAD, finite elements, NURBS, exact geometry and mesh refinement, Comput. Methods Appl. Mech. Engrg. 194 (39–41) (2005) 4135–4195.

[49] R.A. Sauer, T.X. Duong, K.K. Mandadapu, D.J. Steigmann, A stabilized finite element formulation for liquid shells and its application to lipid bilayers, J. Comput. Phys. 330 (2017) 436–466.

[50] Y.B. SudhirSastry, Y. Krishna, P.R. Budarapu, Parametric studies on buckling of thin walled channel beams, Comput. Mater. Sci. 96 (2015) 416–424.

[51] Y.B. SudhirSastry, P.R. Budarapu, N. Madhavi, Y. Krishna, Buckling analysis of thin wall stiffened composite panels, Comput. Mater. Sci. 96 (2015) 459–471.

[52] P.R. Budarapu, S. Kumar, B.G. Prusty, M. Paggi, Stress transfer through the interphase in curved-fiber pullout tests of nanocomposites, Composites B 165 (2019) 417–434.

[53] F. Roohbakhshan, R.A. Sauer, Isogeometric nonlinear shell elements for thin laminated composites based on analytical thickness integration, J. Micromech. Mol. Phys. 1 (03n04) (2016) 1640010.

[54] R.A. Sauer, T.X. Duong, C.J. Corbett, A computational formulation for constrained solid and liquid membranes considering isogeometric finite elements, Comput. Methods Appl. Mech. Engrg. 271 (2014) 48–68.